THESIS FOR THE DEGREE OF LICENTIATE OF ENGINEERING

Flow Characterization in Bubbling Fluidized Beds with Solids Crossflow

MUNAVARA FARHA

Department of Space, Earth and Environment

CHALMERS UNIVERSITY OF TECHNOLOGY

Gothenburg, Sweden 2024

Flow Characterization in Bubbling Fluidized Beds with Solids Crossflow

MUNAVARA FARHA

© MUNAVARA FARHA, 2024.

Department of Space, Earth and Environment
Division of Energy Technology
Chalmers University of Technology
SE-412 96 Gothenburg
Sweden

Printed by Chalmers Reproservice
Gothenburg, Sweden 2024

Abstract

The present study focuses on the application of bubbling fluidized beds with solids crossflow, which is relevant in processes such as drying, iron ore reduction, pharmaceutical production, and waste incineration. While a uniform distribution of temperature and reactants across the beds can be achieved in a stationary bubbling fluidized bed, the introduction of solids crossflow is typically driven by the need for significant throughput of mass and/or heat transfer across the bed. Moreover, cross flow can aid in stabilizing the fluidization behavior, which is essential for consistent process performance and the scaling up of operations. Despite the critical role of fluidized beds in various industries, understanding their flow characteristics remains a significant challenge for the design and scale-up of new processes. This study aims to explore the behavior of solids flow within a bubbling fluidized bed featuring horizontal crossflow. The research is organized around four key objectives: 1. elucidating the interaction between solid convection and lateral dispersion, 2. analyzing fluidization quality, 3. evaluating the impact of bed-wall friction on solid flow, and 4. assessing the efficiency of solid convection by testing various conveying configurations.

The study employs a cold flow model designed and operated according to the simplified Glicksman scaling laws, using Geldart B-type solids for the investigations. The study evaluates four measurement methods (integral mass accumulation, differential mass accumulation, thermal tracing, and magnetic solids tracing) to assess the solids circulation. Magnetic solids tracing emerges as the preferred technique, as it enables a non-intrusive, continuous, and detailed study of solids transport dynamics. Through this measurement method, a linear correlation was observed between the horizontal solids dispersion coefficient (1×10^{-4}–5×10^{-3} m^2/s) and the mean solids velocity (0–6×10^{-2} m/s), attributed to the enhanced horizontal mixing due to the backmixing induced by the shear flow friction. Rheological analyses confirmed the non-Newtonian, shear-thinning properties of the bed, with wall shear stress ranging from 5–55 Pa·s for wall shear rates within 0.002–4.5 s^{-1}. Lastly, conveying the solids under a controlled bubbling fluidization regime emerged as the most efficient configuration for solids transportation in the studied unit.

Keywords: Fluidization, Bubbling fluidized bed, Solids crossflow, Measurement techniques, Solids mixing, Frictional losses, Solids conveying configuration

List of publications

The thesis is based on the following appended papers, which are referred to in the text by their assigned Roman numerals:

- **I.** Farha, M., Guío-Pérez, D. C., Aronsson, J., Johnsson, F., & Pallarès, D. (2023). Assessment of experimental methods for measurements of the horizontal flow of fluidized solids under bubbling conditions. Fuel, 348. https://doi.org/10.1016/j.fuel.2023.128515
- **II.** Farha, M., Guío-Pérez, D. C., Johnsson, F., & Pallarès, D. (2024). Characterization of the solids crossflow in a bubbling fluidized bed. Powder Technology, 119967. https://doi.org/https://doi.org/10.1016/j.powtec.2024.119967
- **III.** Farha, M., Guío-Pérez, D. C., Johnsson, F., & Pallarès, D. (2024). Frictional losses in a bubbling fluidized bed with horizontal flow of solids. Submitted for publication.
- **IV.** Farha, M., Guío-Pérez, D. C., Johnsson, F., & Pallarès, D. (2024). Comparison of solids conveying configurations for fluidized-bed systems – alternatives to riser. Submitted for publication.

Author contributions:

Munavara Farha is the principal author of Papers I–IV and was responsible for most of the tasks, including experimental work, modeling, data processing, and evaluation. Jesper Aronsson contributed to the conceptualization of Paper I. Research Specialist Diana Carolina Guío-Pérez contributed to the conceptualization, experimental design, review, and discussion of Papers I–IV. Professor David Pallarès contributed to the conceptualization, modeling, review, and discussion of Papers I–IV. Professor Filip Johnsson contributed to the review and discussion of Papers I–IV.

Acknowledgements

I would like to express my heartfelt thanks to my supervisors, David and Carolina, for their constant guidance, support, and encouragement throughout this journey. I am also deeply grateful to my family and friends for their unwavering support and motivation during challenging times.

Lastly, to Freja, my beloved cat, who was just as much a part of this journey as I was.

Munavara Farha

Gothenburg, October 2024

Table of Contents

1. Introduction 9
   - 1.1. Background 9
   - 1.2. Aim and scope 10
   - 1.3. Thesis structure 10

2. Theory 13
   - 2.1. Solids transport mechanisms 14
     - 2.1.1. Transport equations 15
     - 2.1.2. Compartment model 16
   - 2.2. Non-Newtonian granular flow 17
     - 2.2.1. Rheological models 18
     - 2.2.2. Granular flow regime 20
   - 2.3. Fluidization regimes 21

3. Methodology and experimental work 23
   - 3.1. Fluid-dynamic scaling 24
   - 3.2. Experimental setup 25
   - 3.3. Methods utilized for solids flow characterization 26
     - 3.3.1. Integral mass accumulation 28
     - 3.3.2. Differential mass accumulation 29
     - 3.3.3. Thermal tracing 31
     - 3.3.4. Magnetic solids tracing 32
     - 3.3.5. Crossflow fluidized bed rheometry 35
   - 3.4. Solids conveying configurations 36
   - 3.5. Test matrix 38

4. Results and discussion 39
   - 4.1. Evaluation of methods for quantifying solids mean velocity 40
   - 4.2. Characterization of solids transport dynamics 43
     - 4.2.1. Solids mixing 43
     - 4.2.2. Rheological analysis of solids flow 45
   - 4.3. Solids conveying efficiency 48

5. Conclusion 49

6. Future work 51

Nomenclature 53

References 55

1. Introduction

1.1. Background

Fluidization occurs when the behavior of a bulk of solid particles is altered to resemble a fluid-like state through the introduction of a gas or liquid that flows upwards through the solid medium [1]. The fluidization phenomenon is fundamental in modern industrial processes, with applications spanning across the chemical industry, energy and waste management sector, and food industry, highlighting the versatility of this technology. In the chemical industry, the fluidized bed configuration supports the production of polymers and pharmaceuticals by maintaining uniform temperature and composition, thus ensuring high-quality outputs with reduced batch-to-batch variability [1,2]. It enables precise control over particle dynamics and temperature conditions, leading to improved yield and purity. Within the energy sector (pyrolysis/gasification/combustion of solid fuels such as biomass and waste), the ability to handle wide particle sizes and different solids densities allows for efficient energy conversion with high fuel flexibility [1,3]. The homogeneous mixing and temperature distribution maximize conversion efficiency while minimizing undesired emissions (unconverted matter and pollutants) [1]. In the food industry, consistent heating and mixing properties provided by fluidized beds are crucial for processes such as drying or coating, ensuring uniform quality [1,2] and the gentle processing of heat-sensitive ingredients, preserving their nutritional value and flavor.

Within the realm of fluidized bed systems, bubbling fluidized beds (BFBs) and circulating fluidized beds (CFBs) are two predominant configurations. BFBs are characterized by a distinct bubbling behavior where the gas flow induces the formation of bubbles within the bed, promoting efficient gas-solid contact. In the bubbling regime, the gas velocity is sufficient to fluidize and mix the solid particles and provide gas-solids contact, but not so high as to entrain them out of the bed [1,4]. In contrast, CFBs operate at higher gas velocities, resulting in continuous solid circulation throughout the system, which is advantageous for processes requiring high throughput [1,4].

Building on these configurations, dual fluidized beds (DFB) can combine various fluidized bed types, such as CFB-CFB, CFB-BFB, or BFB-BFB, to optimize specific process needs. Typically, DFB systems incorporate at least one CFB to facilitate the circulation of solids. However, the BFB-BFB configuration remains relatively unexplored despite its potential benefits. This configuration offers the possibility of increased compactness and operational simplicity, making it a promising option for applications such as drying, iron ore reduction, pharmaceuticals, and waste incineration [1,2,5,6]. The integration of bubbling beds in DFB systems results in improved control over solids residence time [7,8], efficient solids mixing [9], uniform temperature distribution [10,11], and lower gas compression requirements [12].

While many studies have examined flow characterization in crossflow beds, key knowledge gaps persist regarding the effects of significant solids crossflow in bubbling fluidized beds [13]. The macroscopic horizontal velocity of the solids influences the solids dispersive mixing and thereby solids residence time distributions [14]. This ultimately regulates concentration/temperature gradients [14–16] and the efficiency of chemical reactions [14,17]. Additionally, the impact of solids crossflow on fluidization quality—such as the presence of non-idealities like de-fluidized zones and gas channeling [14,18,19]—is not well understood. Another key aspect is the frictional loss induced by solids crossflow, which increases energy consumption, exacerbates equipment wear, and can impede smooth flow, thus impacting the efficiency and maintenance costs of the system [20]. Lastly, the literature explores the integration of solids crossflow without relying on conventional CFB riser configurations by optimizing fluidization conditions and applying strategic design modifications that vary depending on the industrial application [1,4,21].

However, a systematic assessment and comparison of the performance of these different solids conveying configurations across various fluidization regimes is still lacking.

1.2. Aim and scope

Building on the identified knowledge gaps, this thesis aims to understand the characteristics of solids flow in a bubbling fluidized bed with horizontal solids crossflow. The work is structured around four principal objectives: to describe the horizontal transport of solids; to examine the impact of crossflow on fluidization quality; to characterize the frictional losses associated with solids crossflow; and to investigate various conceptual designs for inducing horizontal convection of solids. Achieving these objectives necessitates accurate measurement of the solids crossflow rate, leading to an additional objective: evaluating different techniques for determining the solids flow rate. The scope of the work is limited to Geldart B-type solids, commonly used in fluidized-bed reactors for thermochemical conversion.

1.3. Thesis structure

This thesis compiles key findings from four appended papers. As illustrated in **Figure 1**, the investigation begins by evaluating measurement techniques for accurately assessing solids transport mechanisms, encompassing parameters such as solids velocity, dispersion coefficients, mixing characteristics, fluidized bed rheology, and convection efficiency. Paper-I examines four measurement methods for estimating solids circulation flow rate in a bubbling bed with induced horizontal crossflow, ultimately selecting the magnetic solids tracing technique for further study on solids flow characterization. Paper-II examines the combined effects of solids velocity and horizontal dispersion, along with an evaluation of fluidization quality that accounts for system non-idealities. Paper-III addresses the frictional losses associated with solids crossflow by examining bed rheology. Lastly, Paper-IV explores configurations to induce horizontal solids flow, evaluating different configurations for their efficiency, controllability, and operational range.

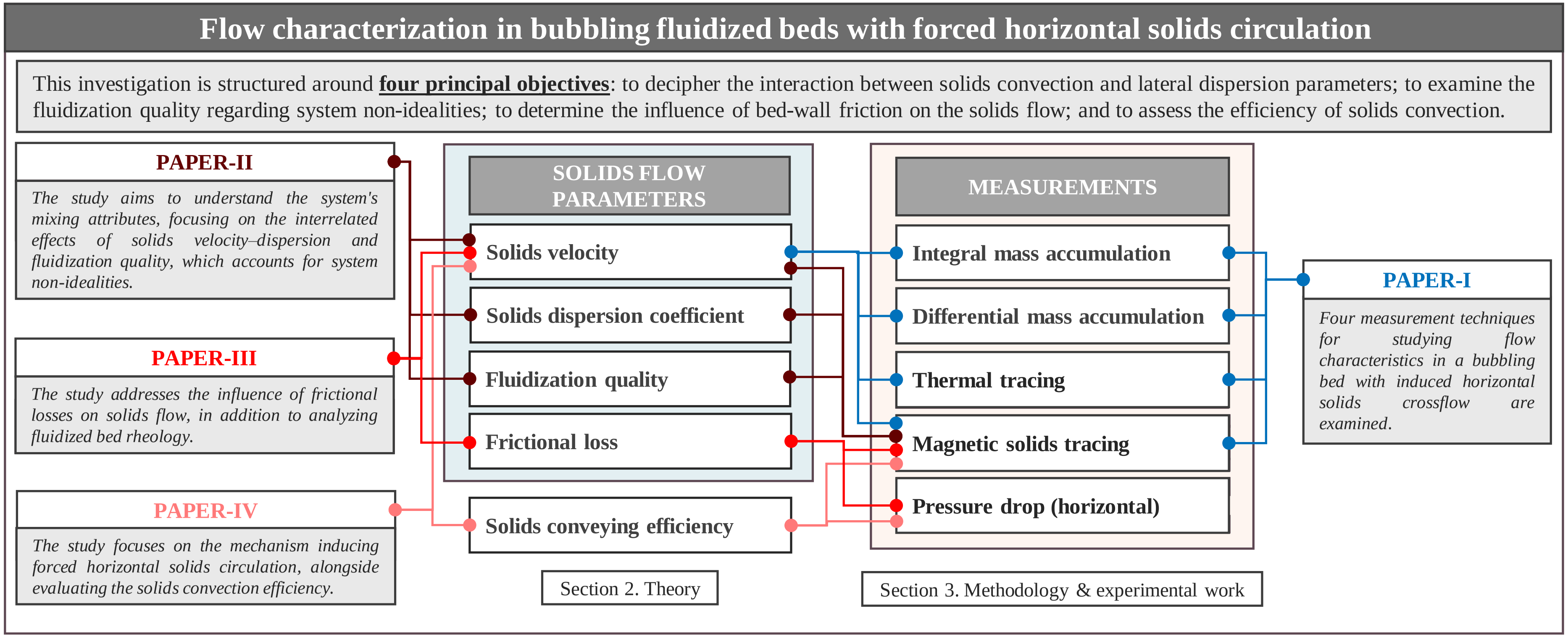

Flow characterization in bubbling fluidized beds with forced horizontal solids circulation

This investigation is structured around **four principal objectives**: to decipher the interaction between solids convection and lateral dispersion parameters; to examine the fluidization quality regarding system non-idealities; to determine the influence of bed-wall friction on the solids flow; and to assess the efficiency of solids convection.

PAPER-II

The study aims to understand the system's mixing attributes, focusing on the interrelated effects of solids velocity–dispersion and fluidization quality, which accounts for system non-idealities.

PAPER-III

The study addresses the influence of frictional losses on solids flow, in addition to analyzing fluidized bed rheology.

PAPER-IV

The study focuses on the mechanism inducing forced horizontal solids circulation, alongside evaluating the solids convection efficiency.

PAPER-I

Four measurement techniques for studying flow characteristics in a bubbling bed with induced horizontal solids crossflow are examined.

SOLIDS FLOW PARAMETERS
Solids velocity
Solids dispersion coefficient
Fluidization quality
Frictional loss
Solids conveying efficiency
Section 2. Theory
MEASUREMENTS
Integral mass accumulation
Differential mass accumulation
Thermal tracing
Magnetic solids tracing
Pressure drop (horizontal)
Section 3. Methodology & experimental work

Figure 1: Summary of the research presented in this thesis, highlighting the main objective of each paper and their arrangement within the overall structure.

2. Theory

This section outlines the fundamental concepts used for solids flow characterization in bubbling fluidized beds with induced solids crossflow. It details the following areas: solids transport mechanisms, encompassing solids velocity, horizontal dispersion, and non-idealities that impact fluidization quality (**Section 2.1**); bed rheology (**Section 2.2**); and fluidization regimes (**Section 2.3**).

2.1. Solids transport mechanisms

The horizontal movement of solids in a bubbling fluidized bed with a solids cross flow is governed by the combined impact of solids dispersion and convection [22–24]. Convection refers to the macroscopic transport of solid particles induced by the solids crossflow [1,4,14]. Horizontal dispersion refers to the spreading and mixing of solid particles due to random motion and interparticle collisions [1,4,14]. This process is typically linked to random walk patterns caused by macroscopic structures, such as those generated by bubble flow in multiphase systems.

Figure 2 illustrates two scenarios of solids transport in fluidized beds with horizontal solids crossflow: a purely convective case (**Figure 2a**) and a case where horizontal dispersion complements the convective movement (**Figure 2b**). Understanding the dynamics of these two transport mechanisms and any interplay between them is essential for accurately characterizing the solids flow. Further, the relative impact of convection and dispersion is expected to vary with operating conditions, bed geometry, and particle characteristics. **Section 2.1.1** outlines the transport equations related to these mechanisms.

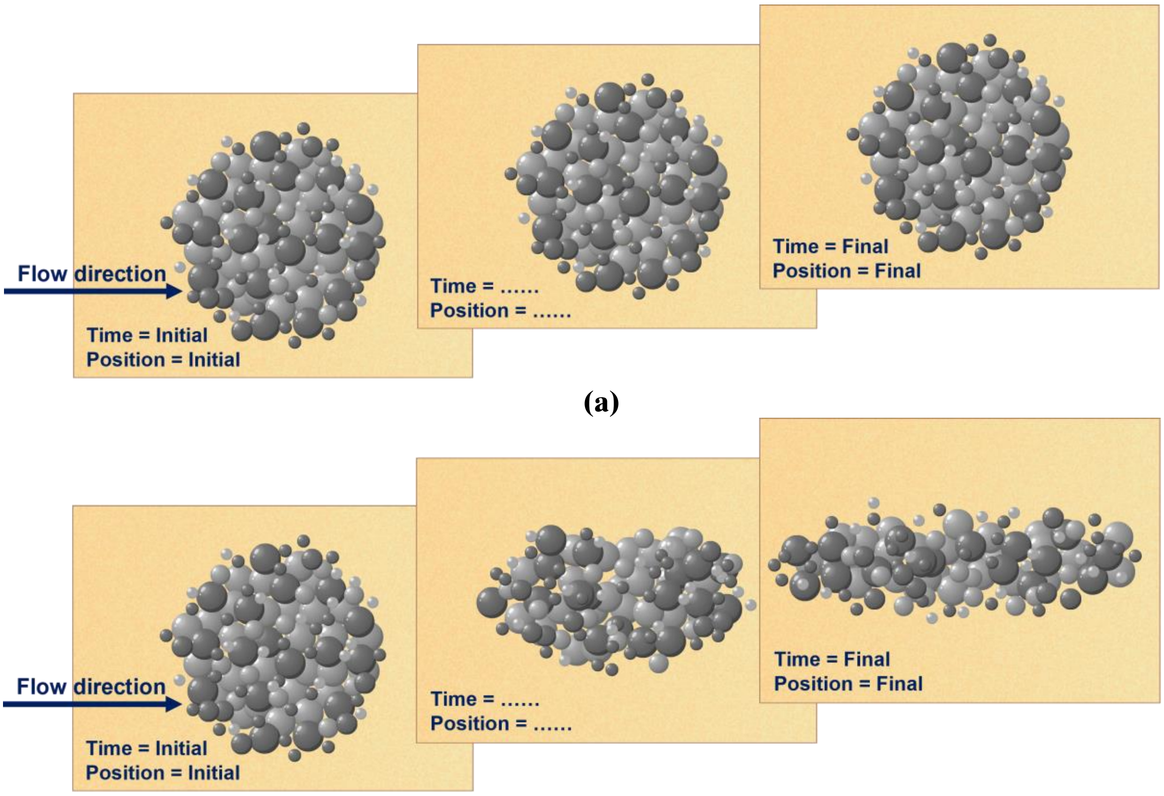

(a)

(b)

Figure 2: Mechanisms of solids transport in a bubbling fluidized bed with induced horizontal flow: (a) pure convective transport, (b) combined convective-dispersion transport.

The solids flow contains a varying extent of non-idealities which yield to a deviation from the description expressed through convection and dispersion. This is the case for dead zones and short-circuiting, which can influence the transport of solids within a fluidized bed. Dead zones are regions within the fluidized bed where solid particles remain largely immobile [14]. Short-circuiting occurs when solids bypass the intended flow path, often due to channel formation, inadequate fluidization, or design flaws, leading to direct movement from inlet to outlet [14]. These scenarios result in poor mixing, uneven residence time distribution, and reduced process efficiency due to insufficient contact between solids and the gas phase. **Section 2.1.2** provides a detailed discussion on the utilization of RTD (residence time distribution) curves to quantify the aforementioned non-ideal characteristics.

2.1.1. Transport equations

Transport equations describe how certain parameters (e.g., mass, momentum, energy) change in space and time. By considering transport terms that represent convection and dispersion, the solids velocity and solids dispersion coefficient are included in the transport equations and can be studied. Two different transport equations are employed to investigate these parameters: the equations for species conservation and energy conservation. In this work, the transport equations are simplified to a 1-dimensional form, with the spatial dimension corresponding to the horizontal direction of solids crossflow, as illustrated in **Figure 3**. This 1-dimensional representation of the flow along the solids flow direction implies a loss of spatial resolution in the directions across the flow, reducing the ability to study parameter gradients due to phenomena such as bed-wall friction.

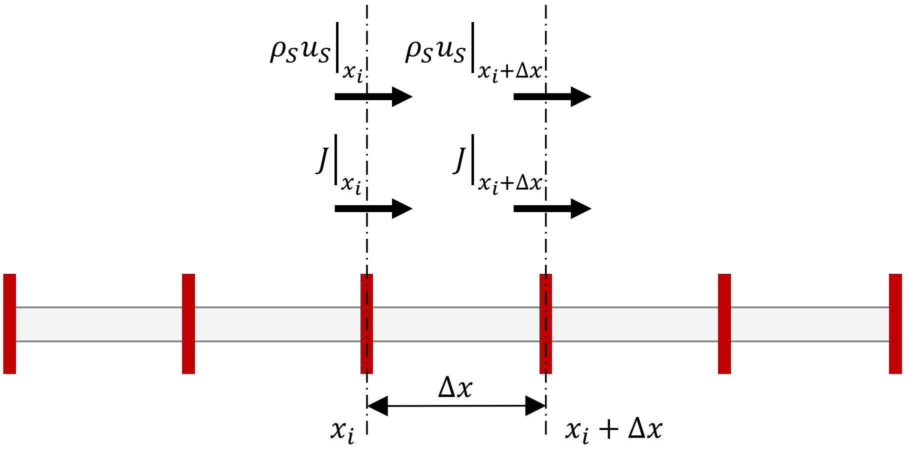

Figure 3: Schematic representation of the species conservation equation applied to a one-dimensional domain along the horizontal direction of solids flow considered in this study.

The species conservation equation describes in its transient form [Eq.(1)] the change in the concentration of a certain species over time and space as a function of the dispersion coefficient D_S and the solids velocity u_S [25].

$$\frac{\partial \rho_S}{\partial t} = D_S \frac{\partial^2 \rho_S}{\partial x^2} - u_S \frac{\partial \rho_S}{\partial x} \tag{1}$$

Additionally, the net flow due to dispersion, or dispersive flux, is described by Fick's first law, which relates the flow of a substance to its concentration gradient and is proportional to the dispersion coefficient [25]:

$$J = D_S \frac{\partial \rho_S}{\partial x} \tag{2}$$

The energy conservation equation models the heat balance across a domain in its stationary form [Eq.(3)] to yield a temperature profile, $T(x)$, as a function of the dispersion coefficient D_S, the solids velocity u_S, and the gas flow parameters included in the rightmost source term [25]:

$$0 = \lambda \frac{\partial^2 T}{\partial x^2} - \{\rho_S \cdot u_S \cdot (1 - \varepsilon_g) \cdot C_{p,S}\} \frac{dT}{dx} + \{\rho_f \cdot u_f \cdot C_{p,F}\} \frac{\Delta T}{H_b} \tag{3}$$

where the effective thermal conductivity of the bed, λ, is linked to the solid's lateral dispersion coefficient, D_S [26]:

$$\lambda = D_S \left(1 - \varepsilon_g\right) \cdot C_{p,S} \cdot \rho_S \tag{4}$$

2.1.2. Compartment model

Reactor design literature contains analytical expressions describing specific ideal flow patterns, e.g., perfectly mixed, plug flow, or stagnant. Although the flow pattern in real systems often deviate from such ideal reactor models, good approximations can be achieved by proper combination of these ideal descriptions. A compartment model aims at representing the flow through a given reactor by interconnecting model subunits [14]. This approach enables the quantification of the extent of different flow patterns, including unwanted phenomena like dead zones, by fitting experimental residence time distribution (RTD) data to the modeled one.

In this study, the compartment model is used to describe the mixing of solids in the direction of the solids crossflow. This is achieved by modeling the process as a series of continuously stirred tank reactors (CSTRs) to represent dispersion, and a plug flow reactor (PFR) to represent convective flow, as illustrated in **Figure 4**. The number of CSTRs in the model indicates the degree of dispersion: a higher number suggests more significant dispersion effects. Conversely, the PFR characterizes the convective flow, where the length or size of the PFR reflects the dominance of convective over dispersive transport. Parameters include the number and volume of CSTRs (N_{CSTR}, V_{CSTR}), the volume of the PFR (V_{PFR}), and an additional stagnant compartment representing dead zones (volume V_d). The dead zones indicate de-fluidized regions that reduce the active flow volume of the solids. Other compartment models can be used to describe the flow in a given system, but the one presented has shown good agreement with the experimental data used in this work.

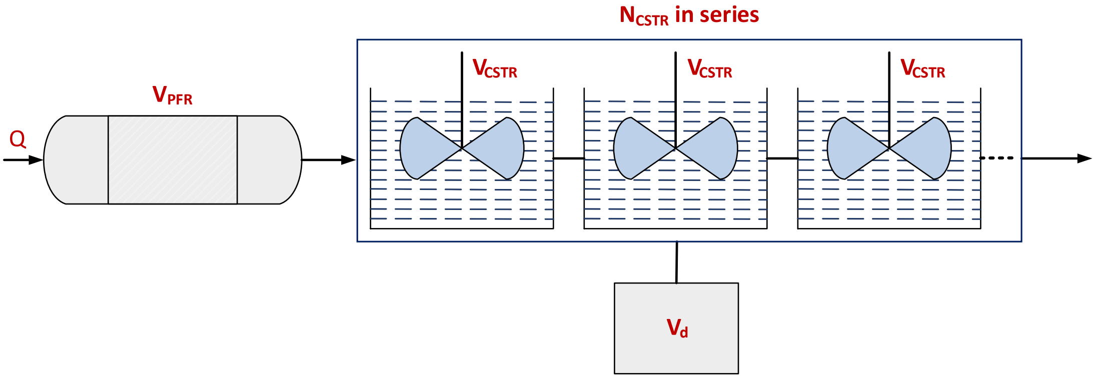

Figure 4: Schematic of the compartment model employed, featuring a PFR, a series of CSTRs, and a stagnant compartment.

Eq.(5) provides the analytical expression providing the transient outlet concentration of a tracer, given the input function of tracer concentration $C_{in}(t)$. M_t and Q_t represents the mass and volumetric flowrate of the tracer injected, τ is the mean residence time of solids, and i_d is the volume share of dead zones (V_d) in the whole system [14].

$$C_{out}(t) = C_{in}(t) + \frac{M_t}{Q_t}\left\{\frac{1}{\tau(1-i_d)}\frac{{N_{CSTR}}^{N_{CSTR}}}{(N_{CSTR}-1)!}\left[\frac{(t-\tau_{PFR})}{\tau(1-i_d)}\right]^{N_{CSTR}-1}\right\}e^{-N_{CSTR}\frac{(t-\tau_{PFR})}{\tau(1-i_d)}} \quad (5)$$

Furthermore, the residence time distribution (RTD) for the solids (also called E-curve) corresponding to the employed compartment model is described by:

$$E(t) = \left\{\frac{1}{\tau(1-i_d)}\frac{{N_{CSTR}}^{N_{CSTR}}}{(N_{CSTR}-1)!}\left[\frac{(t-\tau_{PFR})}{\tau(1-i_d)}\right]^{N_{CSTR}-1}\right\}e^{-N_{CSTR}\frac{(t-\tau_{PFR})}{\tau(1-i_d)}} \quad (6)$$

2.2. Non-Newtonian granular flow

Non-Newtonian fluids [27] exhibit complex behaviors where their apparent viscosity changes in response to the shear rate applied, diverging from Newtonian fluids (which maintain a constant relationship between shear stress and shear rate). **Figure 5** illustrates the distinct rheological behaviors exhibited by different fluid types. Shear-thinning, also known as pseudoplastic behavior, occurs when a fluid's apparent viscosity decreases with an increase in shear rate, making it flow more easily under higher stress. Conversely, shear-thickening, or dilatant behavior, describes a fluid whose apparent viscosity increases with the shear rate, becoming more resistant to flow as higher stress is applied. Further, non-Newtonian flows can exhibit a yield stress, requiring a stress threshold before flowing (red curves in **Figure 5**).

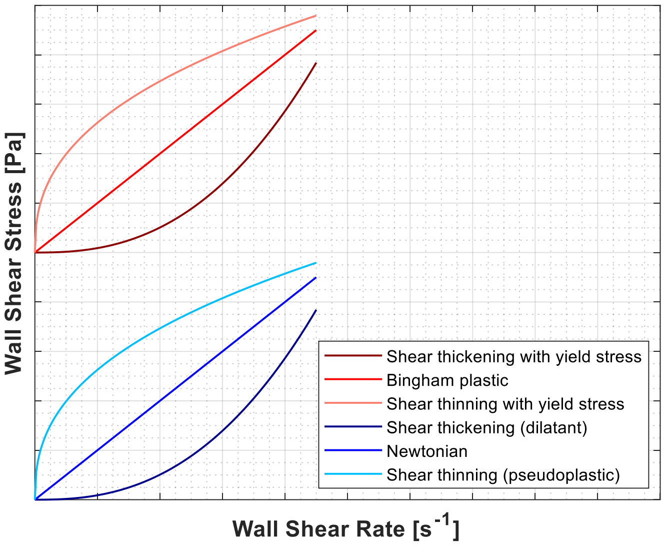

Figure 5: Rheological profiles for different types of fluids.

2.2.1. Rheological models

Gaining insight into the rheology of fluidized beds represents a challenge due to their non-Newtonian characteristics [27,28] and the limited literature available. The rheological properties of fluidized beds have been investigated using various techniques. The falling sphere [28–30] method determines viscosity by tracking the descent of a sphere through the medium, applying Stokes' law. Capillary [28–30] techniques evaluate flow behavior in narrow tubes, utilizing the Hagen-Poiseuille principle. Couette [28–30] flow analysis involves studying fluid dynamics between two moving surfaces to assess shear stress and rate.

For a precise representation of rheological characteristics, the development of comprehensive theoretical models is critical. However, existing models primarily focus on single-phase fluid flow, and there is a gap in assessing how well these models can describe the complex behavior of solids in suspension [27,28]. This study analyzes the flow of solids in a rectangular open channel using three established models— Kozicki et al. [31–34], Delplace-Leuliet [35] and Kostic-Harnett [36,37]. The analytical framework for the cited models is briefly presented below.

Assuming incompressible, steady-state flow under fully developed single-phase conditions, the pressure drop gradient in a channel along the direction of flow, $\Delta P/\Delta L$, relates to the flow velocity (u_S), conduit geometry, and fluid (solids suspension, in this case) properties, through the friction factor (f_F) according to:

$$\frac{\Delta P}{\Delta L} = \frac{2 f_F \rho_f {u_S}^2}{D_h} \tag{7}$$

Further, a force balance analysis allows for the formulation of the equation for the average wall shear stress along the wetted perimeter's contour for generalized fluids flowing in rectangular channels:

$$\tau_w = D_h \cdot \frac{\Delta P}{\Delta L} \tag{8}$$

Previous research on fully developed laminar non-Newtonian fluids has also introduced correlations for specific conduit shapes, e.g., non-circular, that make use of a generalized Reynolds number Re^* and a geometric constant C:

$$f_F = \frac{C}{Re^*} \tag{9}$$

To analyze the rheology of non-Newtonian fluids, the power-law model [Eq.(10)] is employed, which describes the non-linear relationship between wall shear stress and apparent shear rate through the flow behavior index n^* and the flow consistency index k^*:

$$\tau_w = k^* {\dot{\gamma}_a}^{n^*}$$
$$\Rightarrow \tau_w = k^* \left(\frac{8 u_S}{D_h}\right)^{n^*} \tag{10}$$

The apparent shear rate $\dot{\gamma}_a$ is determined under the assumption that the fluid exhibits Newtonian flow characteristics under the given conditions and serves as an initial estimation of the wall shear rate.

The flow behavior of non-Newtonian fluids in non-circular geometries has been previously assessed in the literature using three power-law based rheological models (listed in **Table 1**), which expand on the expressions above to account for the effect of geometry. Kozicki et al. [31] (Model 1) introduced a two-shape-factor (a and b) framework to analyze the flow in rectangular open channels . Kostic-Hartnett [36] integrated concepts from both Kozicki et al. [31–34] and

Metzner-Reed [38], introducing a geometry parameter, ξ, in non-circular ducts. Ayas et al. [37] (Model 2) further refined this approach, specifically targeting its utility for shear-thinning fluids. Delplace-Leuliet [35] (Model 3) noted that while the geometrical coefficients used in those models address the characteristics of non-circular duct, the factor (8^{n-1}) in the denominator is specific to circular ducts and modified this with the introduction of a geometric parameter, β.

Table 1: Rheological parameters in power-law-based models for rectangular channels.

	Model 1	Model 2	Model 3
References	Kozicki et al. [31–34]	Kostic-Hartnett [36]. Further modified by Ayas et al. [37]	Delplace-Leuliet [35]
Reynolds number, Re^* [-]	$\dfrac{\rho_f u_S^{2-n} D_h^n}{8^{n-1} K_{KT} \left[\frac{a+bn}{n}\right]^n}$	$\dfrac{\rho_f u_S^{2-n} D_h^n}{8^{n-1} K_{KH} \xi \left[\frac{3n+1}{4n}\right]^n}$	$\dfrac{\rho_f u_S^{2-n} D_h^n}{\beta^{n-1} K_{DL} \left[\frac{24n+\beta}{(24+\beta)n}\right]^n}$
Flow behavior index, n^* [-]	n		
Flow consistency index, k^* [Pa.s^n]	$K_{KT} \left\{\frac{a+bn}{n}\right\}^n$	$K_{KH} \xi \left[\frac{3n+1}{4n}\right]^n$	$K_{DL} \left[\frac{24n+\beta}{(24+\beta)n}\right]^n$
Wall shear rate, $\dot{\gamma}_w$ [s^{-1}]	$\left[\frac{a+bn}{n}\right]\left[\frac{8u_S}{D_h}\right]$	$\xi^{1/n} \left[\frac{3n+1}{4n}\right]\left[\frac{8u_S}{D_h}\right]$	$\left[\frac{24n+\beta}{(24+\beta)n}\right]\left[\frac{\beta u_S}{D_h}\right]$

Alternatively, extending the generalized Rabinowitsch-Mooney model developed by Kozicki et al. [31,32], this work proposes the following formulation for the flow consistency index for non-circular channels:

$$k^* = K[f(W, H_b)]^n$$

$$\Rightarrow k^* = K\left[C_W\left[\frac{W}{d_S}\right] + C_{H_b}\left[\frac{H_b}{d_S}\right]\right]^n \tag{11}$$

where C_W and C_{H_b} are experimental constants indicating the impact of channel width and bed height on the rheological behaviour of the fluidized solids.

2.2.2. Granular flow regime

The rheologic behavior of a solids suspension strongly depends on the granular regime governing the flow. Therefore, knowing the granular flow regime under which measurements are performed is crucial for establishing the validity limits of the qualitative findings, proposed expressions, and parameter values. At relatively low levels of particle movement, the quasi-static regime is established, where particle-particle interactions are dominated by friction, causing the solids phase to exhibit minimal friction variation and behave in a solid-like manner. As particle movement increases, the intermediate regime is established, where both friction and particle collisions significantly influence the resulting rheology of the solids, leading to a dense, liquid-like flow behavior in the solids phase. With a further increase in particle movement, the collisional regime is reached, where particle collisions dominate the solids phase, inertial effects become prominent, and the friction coefficient stabilizes or decreases as particle collisions become more prevalent, reducing the influence of confining pressure on flow behavior.

The $\mu(I)$ constitutive law, as expressed in Eq.(12), provides an analytical framework to describe the transition of granular flow from a quasi-static regime to a collisional regime as solids movement increases [39–41]. To do so, it describes how the macroscopic friction coefficient, $\mu(I)$, increases with the inertial number, I:

$$\mu(I) = \mu_S + \frac{\mu_2 - \mu_S}{I_0/I + 1} \tag{12}$$

where μ_S is the static friction coefficient, μ_2 represents the friction coefficient at high inertial numbers, and I_0 is a constant. The macroscopic friction coefficient [41,42] is defined as the ratio of the wall shear stress τ_w to the normal stress (or) particle pressure P_p. The inertial number [41,42] quantifies the flow state by comparing two timescales: the particle inertia time, which indicates particle rearrangement, and the deformation time under shear:

$$I = \frac{t_P}{t_{\dot{\gamma}_w}} = \frac{\sqrt{\rho_S d_S^2 / P_p}}{1/\dot{\gamma}_w} \tag{13}$$

2.3. Fluidization regimes

This work explores alternatives to driving solids flow beyond the conventional use of a riser. For this, several solids conveying configurations are tested in this work, each designed to exploit the specific features of gas-solids interactions that characterize the different fluidization regimes. A brief description of the flow characteristics of these fluidization regimes is provided below.

Fluidization regimes represent the different behavioral states (in terms of distinct patterns of particle-fluid interaction) observed when a fluid (a gas in this work) passes through a bed of solid particles [1,4]. The transition from one regime to another is primarily influenced by the fluid velocity, particle characteristics, and fluid properties. **Figure 6** depicts the distinct fluidization regimes achieved as gas velocity is increased. At low gas velocities, the system is in a fixed bed state, where particles remain stationary, and gas flows through the interstitial voids in the bed. As the gas velocity increases to a threshold value, the system reaches the minimum fluidization state, where the gas-solids mixture exhibits fluid-like behavior without the presence of bubbles. Further increase in gas velocity leads to the bubbling fluidization regime, characterized by the formation and ascent of gas bubbles through the bed, which enhances solids mixing. Depending on the bed geometry (e.g., narrow and tall beds), the system may enter the slugging regime, where bubbles grow large enough to occupy the entire cross-section of the bed, causing the bed to behave more like a plug flow reactor. As the gas velocity increases beyond the bubbling regime, turbulent fluidization is achieved, where individual bubbles are no longer distinguishable, resulting in a highly mixed state with intense particle-gas interactions. With further increase in velocity, the system transitions to the fast fluidization regime, marked by partial particle entrainment and a dense upward flow typical of circulating fluidized bed (CFB) systems. Finally, at the highest velocities, the system reaches the lean phase fluidization regime, also known as pneumatic transport, where particles are entrained by the gas flow and move rapidly as dispersed elements.

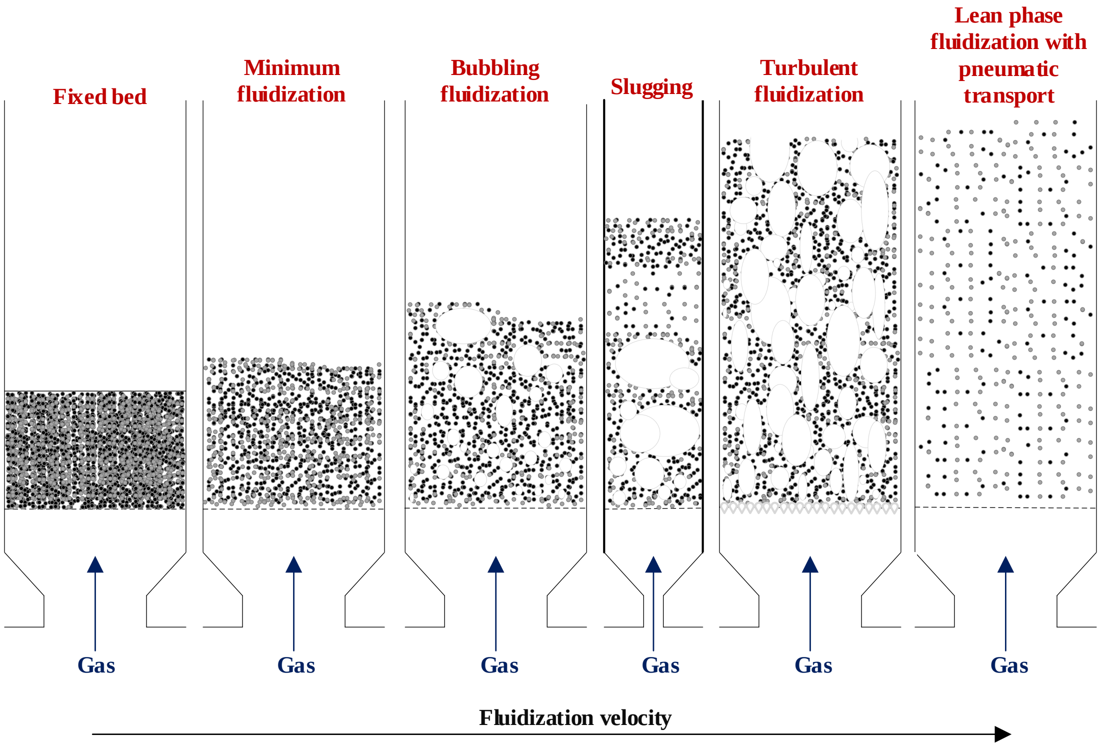

Figure 6: Fluidization regimes established by varying fluidization velocity.

The efficiency of solids convection is determined by the ratio of the energy flow contained in the horizontally conveyed fluidized solids to the energy flow introduced into the solids conveying device in the form of gas:

$$\eta = \frac{E_S}{E_{CZ}} \tag{14}$$

The energy flow imparted to the effective net horizontal flow of solids is determined by the flow rate and the pressure drop in the direction of the solids flow:

$$E_s = u_S \cdot A_{MZ} \cdot \Delta P_{TZ} \tag{15}$$

The energy flow inputted with the conveying gas is defined as [1]:

$$E_{IN} = \frac{\gamma}{\gamma - 1} P_{Atm} Q_{CZ} \left[\left(\frac{P_{Plenum}}{P_{Atm}} \right)^{\frac{\gamma-1}{\gamma}} - 1 \right] \tag{16}$$

3. Methodology and experimental work

This chapter is organized into five sections. **Section 3.1.** presents the methodology used for fluid-dynamic scaling applied in this study, while **Section 3.2.** describes the experimental setup employed. **Section 3.3.** introduces the methods used for solids flow characterization. **Section 3.4.** elaborates on the experimental setup for investigating various configurations for forcing the convection of solids in the horizontal direction. Lastly, **Section 3.5.** outlines the experimental matrix, providing a comprehensive overview of the variables explored.

3.1. Fluid-dynamic scaling

Fluid-dynamic downscaling enables the study of gas-solid flows in large systems operating at high temperatures and/or pressures by replicating their behavior in small units at room temperature. These cold flow models offer greater operational and geometrical flexibility, simplify the use of diagnostic tools, and result in safer, cost-effective experiments. The scaling approach in this study, based on Glicksman's simplified set of scaling laws [43,44], is based on maintaining specific dimensionless numbers as constant as possible between the represented hot unit and the scaled-down model used.

$$\frac{u_0^2}{gD}, \frac{\rho_S}{\rho_F}, \frac{u_0}{u_{mf}}, \frac{G_S}{\rho_S u_0}, \frac{L_1}{L_2}, \varphi, \mathrm{PSD}$$

This set of simplified scaling laws [43,44] is a validated experimental method [44–46] that substitutes the particle's Reynolds number in the original formulation of the scaling laws (known as the full set of scaling laws [43]) with the u_0/u_{mf} ratio. This substitution allows for greater flexibility in length scaling, as it depends on the minimum fluidization velocity ratio (i.e., the specific combination of solids and gas), as shown in Eq.(16).

$$[L] = \frac{W_{COLD}}{W_{HOT}} = \frac{\left[\frac{u_{mf}^2}{g \cdot Fr}\right]_{cold}}{\left[\frac{u_{mf}^2}{g \cdot Fr}\right]_{hot}} = \left(\frac{\left[u_{mf}\right]_{cold}}{\left[u_{mf}\right]_{hot}}\right)^2 \tag{17}$$

The experimental apparatus used in this work was designed with a length scaling factor of $[L]$=0.12. This choice was influenced by laboratory constraints and bed material availability. The experimental unit is designed to replicate large-scale hot conditions, where silica sand with a mean size of 950 µm is fluidized using flue gases at 800°C.

Table 2 compares the operational conditions and bed materials of the cold flow model with its high-temperature counterpart.

Table 2: Main parameters used in the fluid-dynamically scaled model

Parameter	Units	Hot unit	Cold model
Temperature	℃	800	24
Fluidization gas	-	Air or flue gases	Air
Gas density (ρ_F)	kg/m^3	0.359	1.187
Gas viscosity (μ_F)	m^2/s	1.4×10^{-4}	1.54×10^{-5}
Bed geometry	m	L_{HOT}	$0.12L_{HOT}$
Bed material	-	Silica sand	Bronze
Particle density (ρ_S)	kg/m^3	2650	8770
Mean particle diameter (d_S)	µm	950	125
Gas superficial velocity (u_0)	m/s	$u_{0_{HOT}}$	$\sqrt{0.12}\, u_{0_{HOT}}$
Minimum fluidization velocity (u_{mf})	m/s	0.31	0.074
Solids mean velocity (u_S)	m/s	$u_{S_{HOT}}$	$\sqrt{0.12}\, u_{S_{HOT}}$
Solids dispersion coefficient (D_S)	m^2/s	$D_{S_{HOT}}$	$0.042 \cdot D_{S_{HOT}}$

3.2. Experimental setup

The cold flow model utilized in this study [47], shown in **Figure 7**, operates under bubbling conditions. The model has dimensions of 0.5 m × 0.4 m in footprint and 0.5 m in height. It features a central rectangular area, termed ''center box'', which forms the closed annular channel where fluidized solids circulate clockwise under bubbling conditions. As detailed in **Figure 7a,** the annular channel consists of transport zones (where the solids are fluidized under the bubbling regime) and a conveying zone (where the solids crossflow is driven by a combination of high-velocity nozzles and baffles). This setup allows for independent airflow adjustment of the conveying and transport zones.

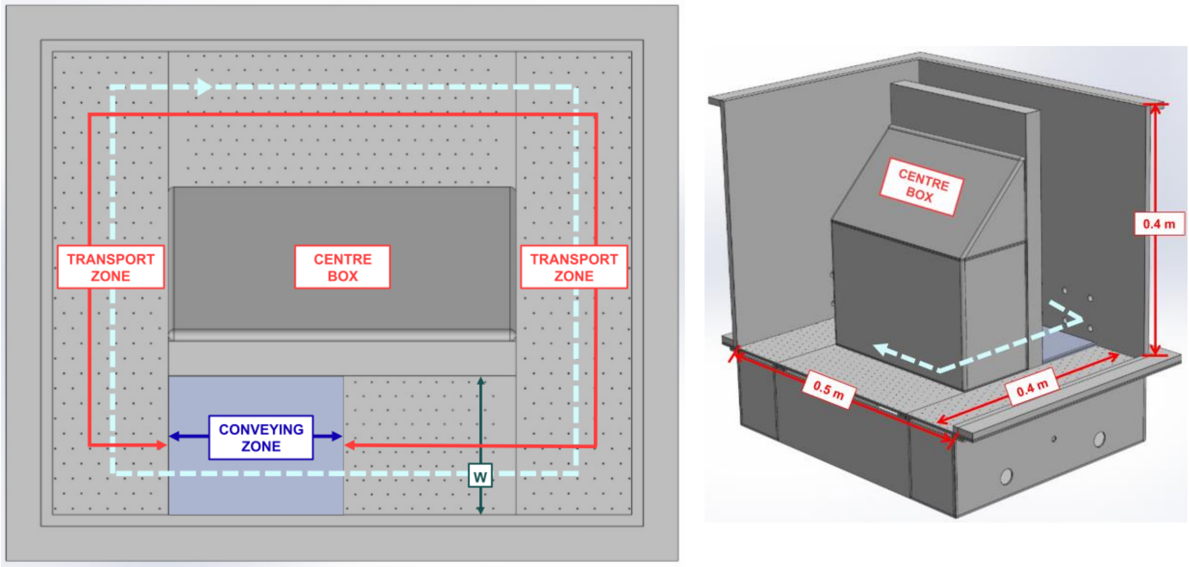

(a) Top view **(b) Isometric view**

Figure 7: Fluid-dynamically down-scaled model with induced clockwise solids circulation.

3.3. Methods utilized for solids flow characterization

Currently, a spectrum of intrusive and non-intrusive measurement methods is available to characterize the flow of solids in fluidized beds.

Intrusive methods directly interact with the bed material, potentially altering the flow they aim to measure. Examples include the mass accumulation [47,48] method, widely used for its efficacy in quantifying solid circulation rates by stopping the flow to accumulate solids over a defined period; optical fiber probes [49], which evaluate local particle velocities or concentrations through the interception of light by particles; hot film anemometers [50] which measures fluid flow velocity via the thermal dissipation effect on a heated element; conductivity probes [51] that detect variations in electrical conductivity as particles interact with the probe, thereby indicating flow rates and bed densities; and thermocouples [52] for capturing thermal gradients within the bed through the principle of thermoelectric effect.

Conversely, non-intrusive techniques maintain the natural state of flow, preferred for their minimal impact on system dynamics. These includes electrostatic induction sensors [53], capturing charge movements induced by particle movement; acoustic emission sensors [54], recording sound waves generated from particle collisions; particle image velocimetry (PIV) [55], a laser-based method visualizing flow by tracking seeded particles; infrared thermography [26,47], visualizing surface temperature distributions by detecting infrared radiation emissions, thereby correlating these emissions to surface temperature variations; radioactive particle tracking [56], traces particle movement within fluidized beds using isotopically tagged particles and radiation detectors to reconstruct their three-dimensional trajectories, leveraging the principles of radioactive decay and detection; magnetic particle tracking [47,57], involves the use of magnetically embedded particles and the detection of their generated magnetic fields to map flow paths; and electrical capacitance tomography (ECT) [58], offering a comprehensive view of internal component distribution by measuring electrical capacitance changes, a technique grounded in the principle that the dielectric properties of materials alter capacitance readings.

In this work, five distinct measurement methods were employed to assess flow parameters: integral mass accumulation, differential mass accumulation, thermal tracing, magnetic solids tracing, and crossflow fluidized bed rheometry. Each method offers unique capabilities, is based on different principles, and has specific requirements for integration into the experiment. Measurement accuracy, unaffected by inherent fluidized bed fluctuations, is ensured through time-averaged calibrations of parameters such as pressure, temperature, and impedance.

The measurement methods, along with the techniques, analytical tools, and solids flow parameters analyzed, are summarized in **Table 3**.

Table 3: Overview of measurement methods, including techniques, analytical tools, and solids flow parameters studied.

Measurement method	Measurement technique	Measured variable	Equation (or) analytical tool used	Extracted variables
Integral mass accumulation	Weight difference	Mass flow rate	$u_S = \frac{\Delta m}{\Delta t} \cdot \left\{\frac{1}{\rho_B \cdot H \cdot W}\right\}$	u_S
Differential mass accumulation	Pressure sampling	Dynamic pressure gradient	$u_S = \frac{dP}{dt} \cdot \frac{A_{Accumulation}}{g} \cdot \left\{\frac{1}{\rho_B \cdot H \cdot W}\right\}$	u_S
Thermal tracing	Thermography	Temperature field (2D)	Transport equation (energy conservation): $0 = \lambda \frac{\partial^2 T}{\partial x^2} - \{\rho_S \cdot u_S \cdot (1 - \varepsilon_g) \cdot C_{p,S}\} \frac{dT}{dx} + \{\rho_F \cdot u_F \cdot C_{p,F}\} \frac{\Delta T}{H_b}$ $D_S = \frac{\lambda}{(1 - \varepsilon_g) \cdot C_{p,S} \cdot \rho_S}$	u_S, D_S
Magnetic solids tracing	Inductance	Transient tracer concentration profile	Transport equation (species conservation): $\frac{\partial C_i}{\partial t} = D_S \frac{\partial^2 C_i}{\partial x^2} - u_S \frac{\partial C_i}{\partial x}$	u_S, D_S
			Compartment model: $C_{out}(t) = C_{in}(t) + \frac{M_t}{Q_t} \left\{ \frac{1}{\tau(1 - i_d)} \frac{{N_{CSTR}}^{N_{CSTR}}}{(N_{CSTR} - 1)!} \left[\frac{(t - \tau_{PFR})}{\tau(1 - i_d)} \right]^{N_{CSTR} - 1} \right\} e^{-N_{CSTR} \frac{(t - \tau_{PFR})}{\tau(1 - i_d)}}$	i_d, N_{CSTR}, τ_{PFR} & τ
Crossflow fluidized bed rheometry	Inductance	Transient tracer concentration profile	Transport equation (species conservation): $\frac{\partial C_i}{\partial t} = D_S \frac{\partial^2 C_i}{\partial x^2} - u_S \frac{\partial C_i}{\partial x}$	u_S
	Pressure sampling	Steady-state pressure gradient	Fanning friction factor: $\frac{\Delta P}{\Delta L} = \frac{2 f_F \rho_f {u_S}^2}{D_h}$	f_F, τ_w, k^*, n^*
			Wall shear stress: $\tau_w = D_h \cdot \frac{\Delta P}{\Delta L}$	
			Power-law model: $\tau_w = k^* \left(\frac{8 u_S}{D_h}\right)^{n^*}$	

3.3.1. Integral mass accumulation

This method aims to obtain the solids mean velocity by the direct measurement of the solids mass conveyed into a container set over a given time. The setup, illustrated in **Figure 8**, uses two boxes to collect the conveyed solids. Box 1, easily removed, collects bed material for solids mean velocity analysis. Box 2, secured tightly against the unit walls, collects any leaked solids, which represent a very small amount compared to those collected in Box 1. The measurement begins with Box 1 sealed by a sliding wall adjacent to the conveying zone. Fluidization is set at the velocities selected for the experiment. After a 30-second stabilization period, the sliding wall is removed, allowing material to be transported to Box 1. The material is accumulated until the box reaches its maximum capacity of 3.5 kg. This weight determines the test duration, inversely related to the solids-conveying rate. After reaching the target weight, Boxes 1 and 2 are retrieved and weighed to assess the solids mean velocity.

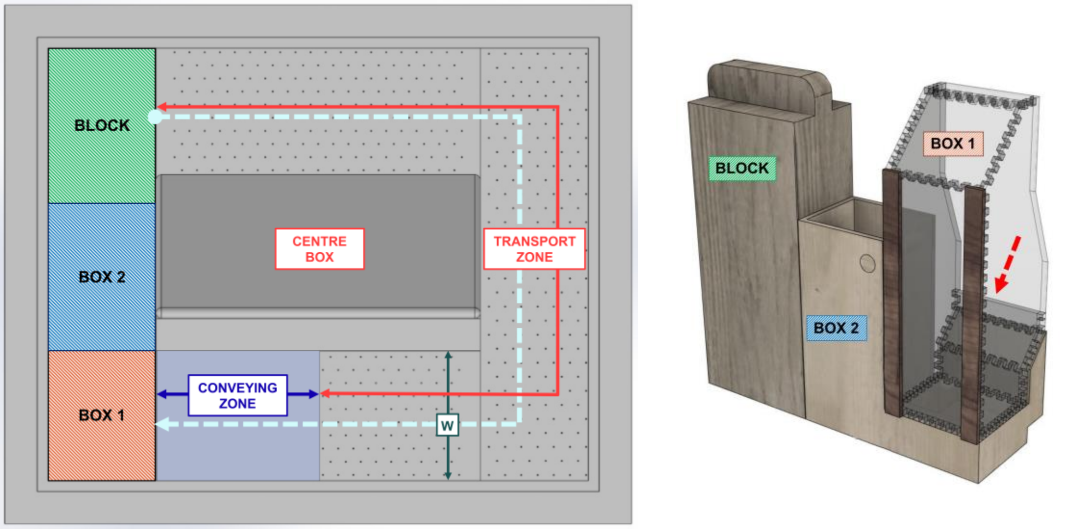

(a) Top view of the unit setting

(b) Box-block arrangement used in the transport zone

Figure 8: Experimental setup used for integral mass accumulation.

The time-averaged solids velocity can be determined as:

$$u_S = \frac{\Delta m}{\Delta t} \cdot \left\{ \frac{1}{\rho_B \cdot H \cdot W} \right\} \tag{18}$$

This method has limitations due to its non-steady nature. The continuous decrease in the inventory of fluidized solids results in a varying bed height, which affects the solids flow rate. Additionally, the length of the circulating loop influences the solids circulation rate, with shorter distances from the accumulation box likely yielding higher flow rates. Since part of the unit's volume is occupied by the collecting boxes, the available volume for solids is reduced, making the conditions less representative of the actual circulating conditions during regular operation of the unit.

3.3.2. Differential mass accumulation

This method involves allowing the conveyed solids to enter a stationary bubbling bed, where the transient pressure build-up resulting from the increased bed height is monitored. To implement this, a wall separator is vertically inserted along guide rails in the transport zone once steady-state conditions are achieved, as shown in **Figure 9a**. This action creates an accumulating bed (blue section) while the remainder of the bed (green section) empties. The resulting pressure change dP in the accumulating bed is then used to quantify the mean velocity of the conveyed solids, according to:

$$u_S = \frac{dP}{dt} \cdot \frac{A_{Accumulation}}{g} \cdot \left\{ \frac{1}{\rho_B \cdot H \cdot W} \right\} \tag{19}$$

Pressure is monitored at three levels in both the accumulating and emptying beds: in the air plenum, and at 5.25 cm and 7.5 cm above the gas distributor. **Figure 9b** exemplifies the pressure transients from these measurements. The stabilization of pressure over time indicates that maximum material accumulation has been reached. The mean velocity of conveyed solids is calculated using the time derivatives of the pressure signals, focusing on the interval where the pressure gradient is constant. The pressure signals from the accumulating bed are used rather than those from the emptying bed for two reasons. First, the accumulating bed, with its smaller cross-section, exhibits a sharper pressure gradient for a given mass flow rate compared to the emptying bed. Second, the accumulating bed is fluidized by a single air plenum, ensuring uniform conditions, whereas the emptying bed has multiple plenums, which may cause some heterogeneity in fluidization.

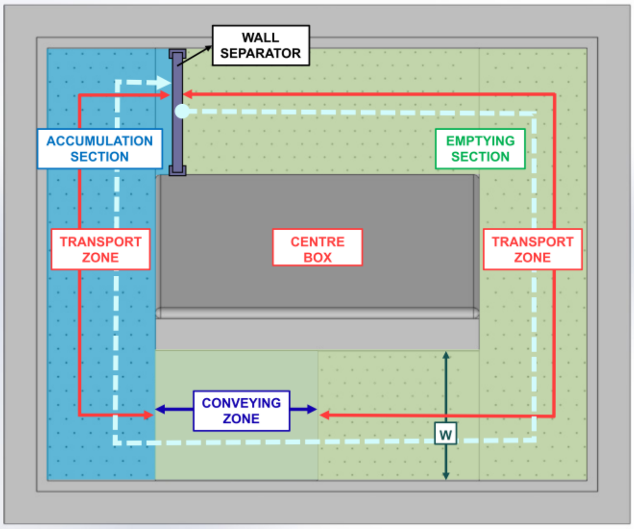
WALL SEPARATOR
ACCUMULATION SECTION
EMPTYING SECTION
TRANSPORT ZONE
CENTRE BOX
TRANSPORT ZONE
CONVEYING ZONE
W

(a) Top view of the unit setting

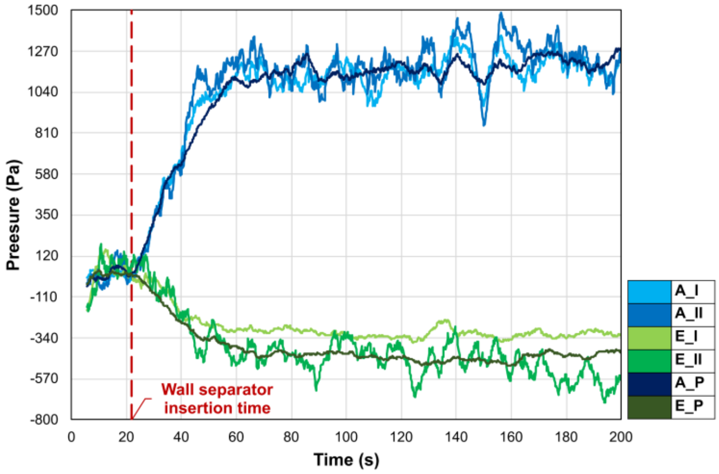

(b) Transient pressure profiles

Figure 9: Experimental setup used for the differential mass accumulation method with associated results. Conditions: FN_{TZ} 3; H 0.08 m and Q_{CZ} 0.0143 m^3/s. 'A' represents the accumulation section, 'E' the emptying section, and 'P' the plenum box. Pressure probes I and II are positioned 7.5 cm and 5.25 cm from the perforated plate, respectively.

The main advantages of this method are its operational simplicity and the use of a time-resolved signal. However, accurate pressure measurement is crucial, especially at low solids flow rates where slow accumulation results in minimal pressure changes. Minor leakages from the accumulating to the emptying zone at high solids convection rates, observed across wall-separator gaps, are visually estimated to have negligible impact on results. Nevertheless, this method uses non-steady conditions and, therefore, has some inherent inaccuracies.

3.3.3. Thermal tracing

This non-intrusive method involves heating circulating solids by fluidizing them with air at 80°C in a section of the circulating loop called 'heating zone' (**Figure 10a**) and cooling them in other sections of the loop fluidized with ambient air. This creates a spatial temperature gradient along the direction of solids flow, which facilitates the determination of the solids mean velocity. The experimental temperature profile is obtained using thermal imaging from the bed surface, resulting in a 2D temperature field that is integrated along the y-direction to produce a 1D profile for model fitting. The modeling uses the energy equation (refer to **Section 2.1.1**) in its 1D steady-state form, discretized using the finite volume method, to determine the solids' horizontal velocity that best fits the temperature profile, $T(x)$ [Eq.(3)], to the experimental data. For each experiment, the dispersion coefficient, D_S, is initially determined under bubbling conditions in absence of solids crossflow [Eq.(4)], allowing for the determination of λ as the sole unknown. **Figure 10b** shows the experimental and modeled profiles for determination of solids dispersion (red curves) and solids convection (blue curves). Boundary conditions are established using in-bed temperature measurements at the beginning (T_0) and end (T_L) of the measuring zone.

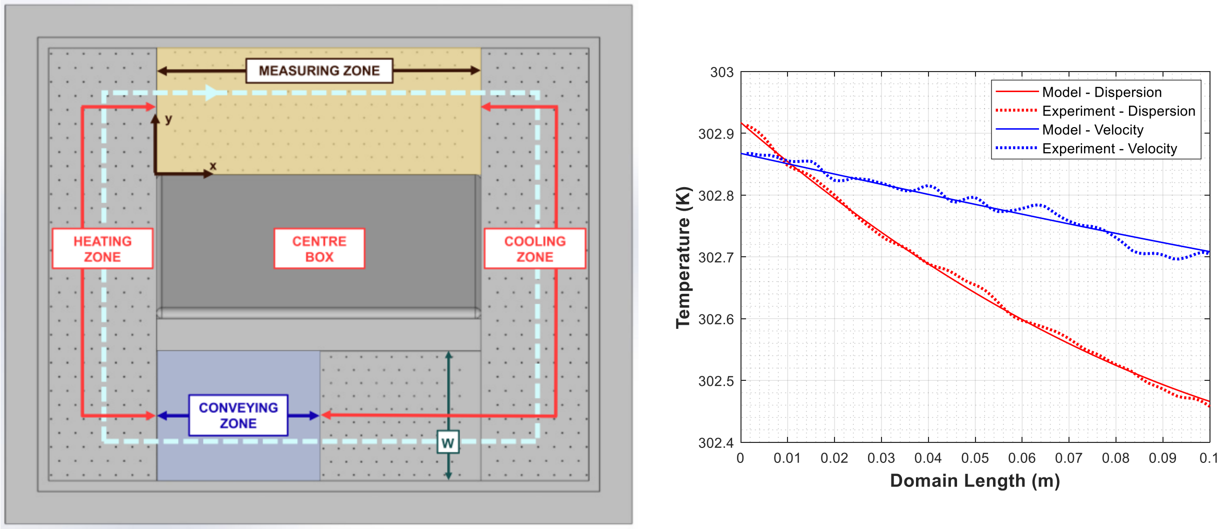

(a) Top view of the unit setting

(b) Experimental and modeled temperature profiles in the absence/presence of macroscopic solids convection.

Figure 10: Experimental setup used for thermal tracing with associated results. Conditions: FN$_{TZ}$ 3; H 0.08 m and Q$_{CZ}$ 0.0143 m^3/s. The temperature scale used is in K.

Note that the lateral dispersion coefficient of solids is assumed constant for the specific fluidization velocity and bed height, regardless of the horizontal solids flow rate. However, this assumption was later found to be incorrect, leading to an overestimation of the calculated solids mean velocity. Further details are discussed in **Section 4.1.**

This study employs several strategies to minimize flow and temperature fluctuations' impact on the measured temperature field: precise control of the fluidization velocity, maintenance of consistent ambient conditions, uniform heating/cooling rates, ensuring a sufficiently large temperature gradient throughout the measuring zone, and utilizing a thermographic camera with high sensitivity (around 0.04 K). However, this sensitivity declines at higher solids flow rates, impacting the method's accuracy. Regarding the limitations of the technique, higher flow rates introduce greater inaccuracies due to thermal inertia, wall friction, unit geometry, and bubble eruption effects, which impact the surface temperature and emissivity of fluidized bed particles.

3.3.4. Magnetic solids tracing

In this technique, a tracer material that is fluid-dynamically similar to the bed material is introduced into the system. **Table 4** presents the physical properties of the materials along with their dimensionless particle size based on Archimedes' number.

Table 4: Comparison of the bed material and magnetic tracer.

Parameter	Unit	Bed	Tracer
Material	-	Bronze	Fe-based alloy
Particle density (ρ_S)	kg/m^3	8,770	7,988
Bulk density (ρ_B)	kg/m^3	5,522.1	4,520
Particle size distribution			
d_{10}-d_{50}-d_{90}	µm	80-112-132	25-69-123
Sauter mean diameter (d_{32})	µm	126	102
Archimedes' number, Ar$^{1/3}$	-	8.386	6.127
Minimum fluidization velocity (u_{mf})	m/s	0.074	0.039
Magnetic susceptibility	-	0	0.9

Pulse tracer measurements are conducted using four inductance coils, each covering the entire solids flow cross-section (as illustrated in **Figure 11a**) located along the solids measuring zone to monitor the varying tracer concentration. A batch of iron-based tracer material is introduced at the tracer injection point, 14 cm upstream of the first coil (C1), as shown in **Figure 11**. The transient tracer concentration is sampled, allowing for the computation of the tracer residence time distribution, which enables the calculation of the solids' horizontal flow and dispersion rates. **Figure 11b** depicts the characteristic transient responses of raw concentration signals obtained from coils C1 to C4 during a tracer experiment.

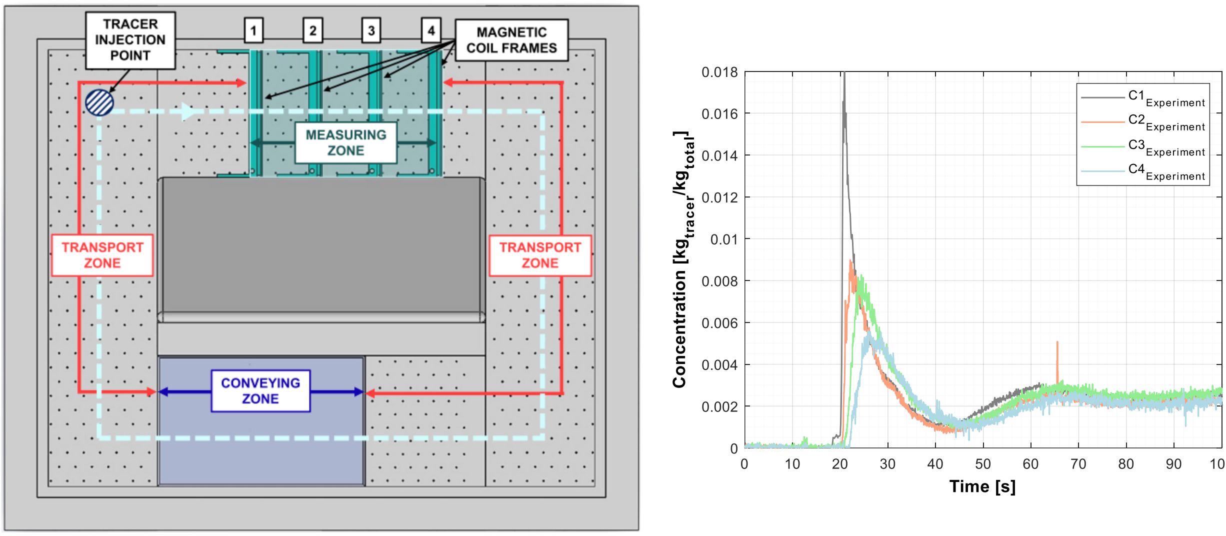

(a) Top view of the unit setting

(b) Transient profiles of the measured tracer concentration at each coil

Figure 11: Experimental setup used for the magnetic solids tracing method, accompanied by the transient concentration profiles obtained. Conditions: FN$_{TZ}$=3, H=0.08 m, Q$_{CZ}$=0.0143 m^3/s.

The main drawbacks of this method include the time-intensive separation of the magnetic tracer after each experiment and the inability to exactly replicate the physical properties of the bed material with the available tracer materials. Additionally, tracer segregation at unit corners and less distinct coil signals at low circulation rates were observed, affecting the measurement accuracy.

Data from the magnetic solids tracing experiment are analyzed using two analytical approaches: the transient convection-dispersion model (**Section 2.1.1**) and the compartment model (**Section 2.1.2**). Each approach allows for the study of different flow characteristics.

For the first method, the transient convection-dispersion equation (see Eq.(1)) is solved to determine the values of the solids' mean velocity and dispersion coefficients. For the numerical solution, the transient mass balance for the tracer species is solved using the finite volume method, employing a fully implicit discretization scheme for stability and accurate time integration. The hybrid differencing scheme combines central differencing's precision in uniform regions with upwind differencing's stability in areas of steep gradients. The modeled domain extends from the position of coil 1 to the boundary between the transport zone and the solids conveying section. Boundary conditions are set as follows: a transient Dirichlet condition at coil 1 based on the measured tracer concentration, and a zero-gradient condition at the conveying section inlet, simulating a wall that allows convection but not dispersion.

For the second method, parameter fitting employs a non-linear optimization procedure to align the compartment model (see Eq. (5)) predictions with the measured tracer concentrations from the coils. The compartment model treats the signal from coil 1 as the input, and parameter adjustment focuses on reducing differences between predicted and measured signals for coils 2-4. Additionally, a robust fitting strategy tackles multiple local optima by varying initial parameter estimates. The solids flow parameters of interest from this method are the system's non-idealities, such as dead zones.

Figure 12a illustrates an example of the data attained after fitting experimental data with the convection-dispersion model to estimate solids velocity and dispersion coefficient: it compares measured and modeled transient tracer concentration responses at each coil, along with the input from coil 1. The initial tracer batch passage is evident from sharp peaks in the tracer signal at all coils, with coils farther from the injection point showing broader peaks due to increased extent of the dispersive mixing. A subsequent decrease in tracer concentration and a lower secondary peak follow, marking the next tracer loop around the unit. Eventually, the curves converge to a stable state, indicating uniform tracer distribution throughout the circulating loop.

Figure 12b presents the residence time distribution (RTD) curves derived from compartment model fitting. Coil 1 serves as domain inlet, with the subsequent three coils acting as respective outlets. As observed, the RTD curve shifts and broadens as the tracer progresses through the transport zone, indicating an increase in mean residence time and (extent of) dispersion as the tracer moves from one outlet coil to the next.

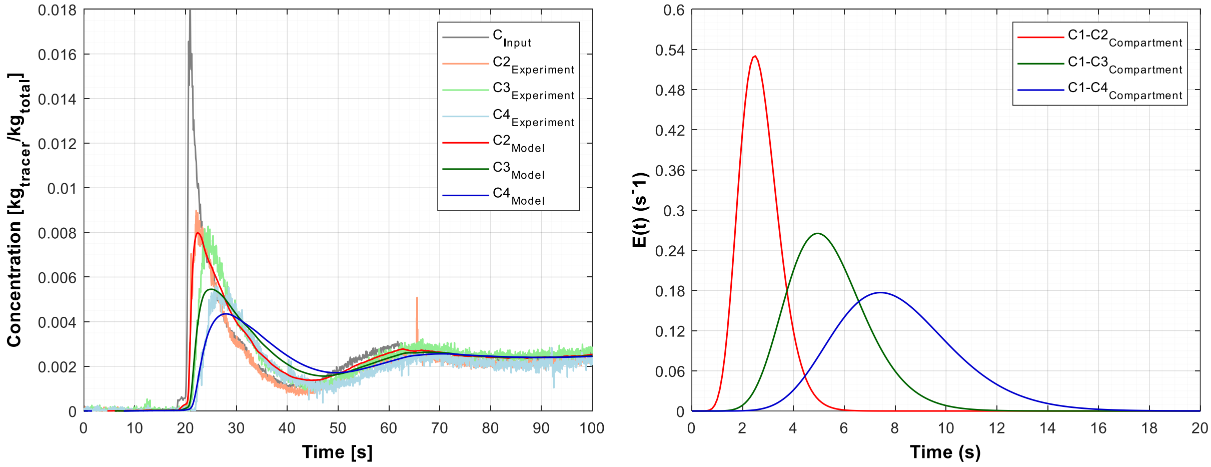

Fitted variables:
u_S=1.35×10^{-2} m/s, D_S=1.64×10^{-3} m^2/s

(a)

Fitted variables:
i_d=0.07, N_{CSTR}=6, τ=5.16 s, τ_{PFR}=0.3 s

(b)

Figure 12: Analysis outcomes from magnetic solids tracing technique. (a) Transient profile of the measured tracer concentration, alongside the convection-dispersion model fitting. (b) Residene time distribution curves obtained from compartment model fitting. Conditions: FN$_{TZ}$=3, H=0.08 m, Q$_{CZ}$=0.0143 m^3/s.

3.3.5. Crossflow fluidized bed rheometry

The determination of the solids velocity parameter utilizes the magnetic solids tracing technique, with the coil placements depicted in **Figure 13a**, adjacent to the injection probe location. Additionally, two pressure probes are positioned within the measuring zone, as shown in **Figure 13a**: one upstream of coil 1 and another downstream of coil 4. These measurements—solids velocity and pressure drop along the transport channel in the horizontal direction of solids flow—are integral to a quantitative mechanistic analysis aimed at elucidating frictional losses and the rheological properties of the bed. The assessment of frictional losses also considers experiments with varying channel widths achieved by extending the central box, as shown in **Figure 13b**.

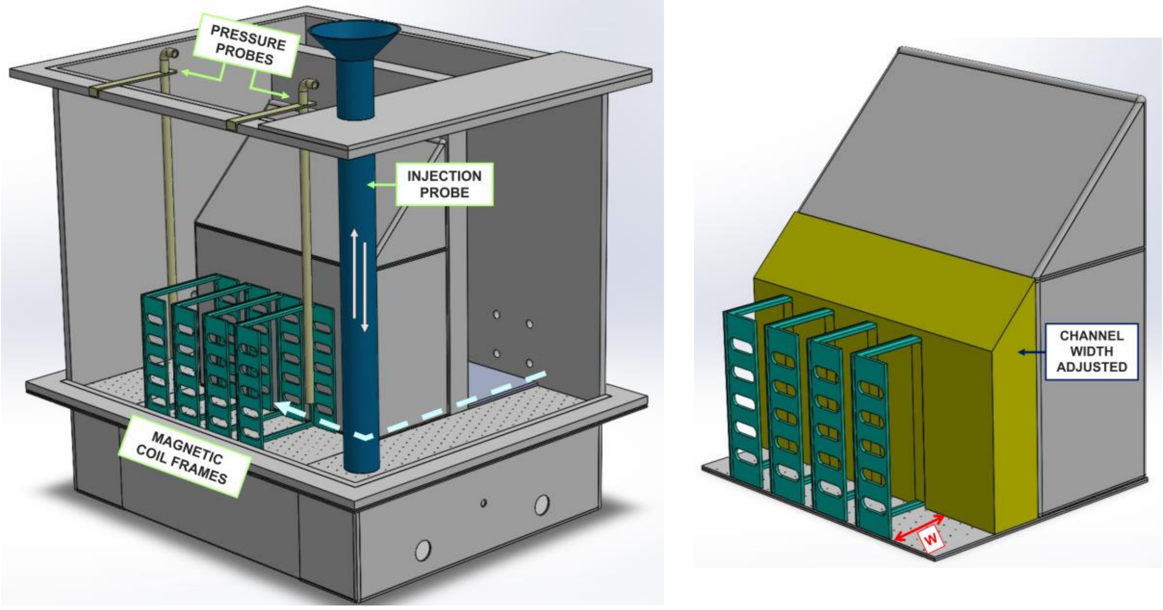

(a) **(b)**

Figure 13: Schematic of the CFM setup configuration designed for the study of frictional losses in the direction of solids crossflow, indicating (a) the positions of pressure probes within the measuring zone, and (b) depiction of adjustments made to the channel width.

Three key parameters are measured: bed voidage [47], pressure drop gradient along the solids flow, and solids velocity (**Section 3.3.4.** Based on the pressure and velocity data, Fanning friction factor and wall shear stress are calculated using Eq.(7) and Eq.(8), respectively. Using the power-law model as reference, the relationship between wall shear stress and apparent shear rate for the specific system under study is elucidated [Eq.(10)], also facilitating the determination of flow behavior and consistency indices.

Lastly, the $\mu(I)$ constitutive law [Eq.(12)] was used to quantify the frictional behavior of the bed, where the macroscopic friction coefficient, $\mu(I)$, was determined from wall shear stress based on the pressure drop gradient measured.

3.4. Solids conveying configurations

The achievement of stable and controllable convection of solids in the horizontal direction has remained under-researched. Although some configurations have been proposed [21], their performance needs to be assessed in terms of range, controllability and efficiency. In this work, five different configurations are tested for their ability to convey solids horizontally. The configurations tested are illustrated in **Figure 14**: (a) Free solids splashing, (b) Confined solids splashing, (c) Slugging, (d) Solids entrainment, and (e) Directed gas injection.

The free solids splashing configuration functions under the 'bubbling fluidization' regime, where particles mainly reside in a dense phase and are lifted by ascending gas bubbles. Upon reaching the surface, these bubbles burst, ejecting solids into the air in a process known as splashing [4]. This results in high velocities and a wide range of ejection angles, leading to a ballistic backmixing pattern of solids. [4,59,60]. The free solids splashing configuration (**Figure 14a**) confines the injected conveying gas for bubble formation using a barrier threshold from nozzle level to the dense bed surface and a hanging baffle that partially immerses in the dense bed, leaving space for solids entry. This setup allows some solids splashing in the module to cross the threshold, creating a net solids flow. Additionally, a roof is installed to direct splashing solids in the desired direction.

The confined solids splashing configuration employs the 'turbulent fluidization' regime, which is marked by chaotic particle motion due to the gas phase's high kinetic energy [4,59]. Particle transport occurs via turbulent gas eddies and bubble buoyancy [4,59]. The confined solids splashing configuration (**Figure 14b**) utilizes a geometry with narrower lateral confinement than the free solid splashing.

The slugging configuration induces the formation of slug-like gas voids through bubble coalescence [4]. The drag forces from rising slugs, coupled with gravitational settling, yield a recirculation pattern within the bed, leading to a pronounced pulsating flow [4,59,61]. The slugging configuration (**Figure 14c**) features a specialized module with six smaller bed columns in the conveying zone, each designed to simulate slug formation.

The solids entrainment configuration utilizes the phenomenon where solids are lifted vertically from the dense bed by the gas stream. This effect intensifies at higher gas velocities seen in turbulent, fast fluidization, and pneumatic regimes [1,4]. With increased velocities, the separation between dense and dilute solids phases blurs, with the gas predominantly moving in jet streams rather than distinct bubbles [1,4,59]. This significant gas-driven drag of solids often necessitates the use of downstream separation devices like cyclones [1,4,59]. The corresponding configuration (**Figure 14d**) increases gas velocity to facilitate the upward movement of particles and features a gas-solids separator at the top of the module. This separator collects and redirects entrained solids into the unit's transport zone, thereby inducing a flow of solids.

Lastly, in the directed gas injection configuration, the angled nozzles inject fluidizing gas to impart a horizontal trajectory to the gas bubbles. This action, in turn, induces horizontal movement of the solids by dragging them along this directional path. The configuration (**Figure 14e**) uses five rows of nozzles, each set at specific inclination angles.

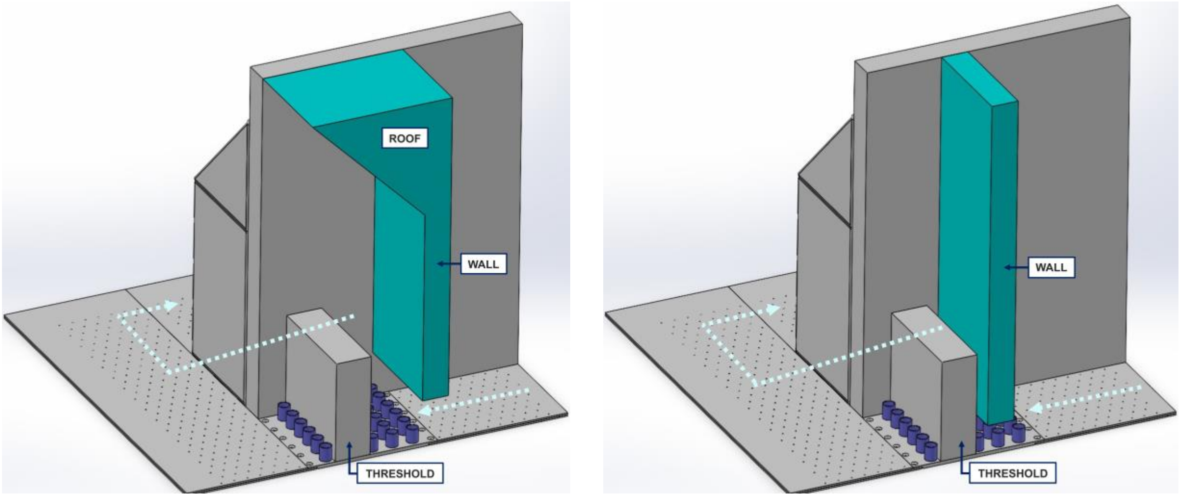
ROOF
WALL
THRESHOLD
WALL
THRESHOLD

(a) Free solids splashing **(b) Confined solids splashing**

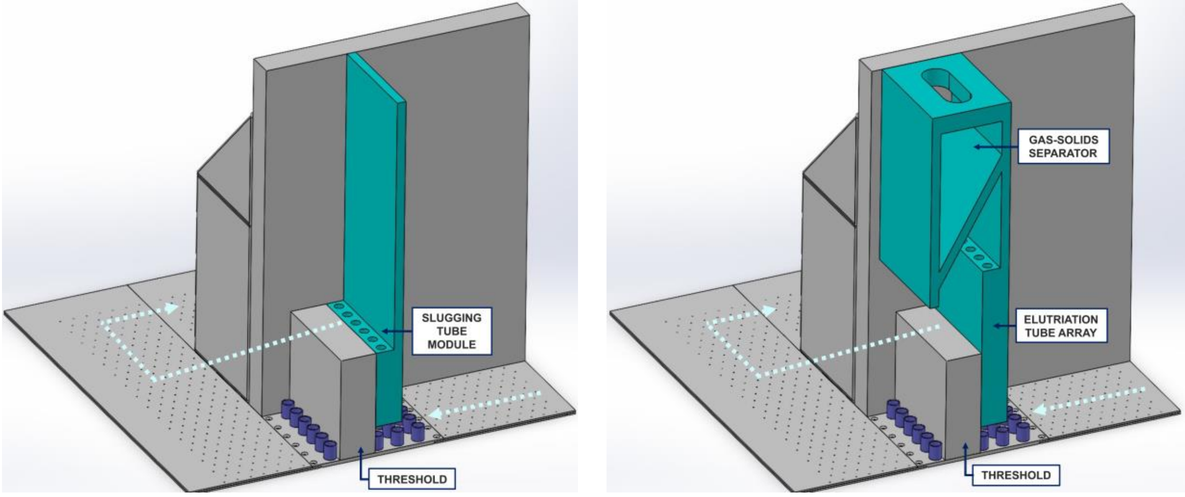
SLUGGING TUBE MODULE
THRESHOLD
GAS-SOLIDS SEPARATOR
ELUTRIATION TUBE ARRAY
THRESHOLD

(c) Slugging **(d) Solids entrainment**

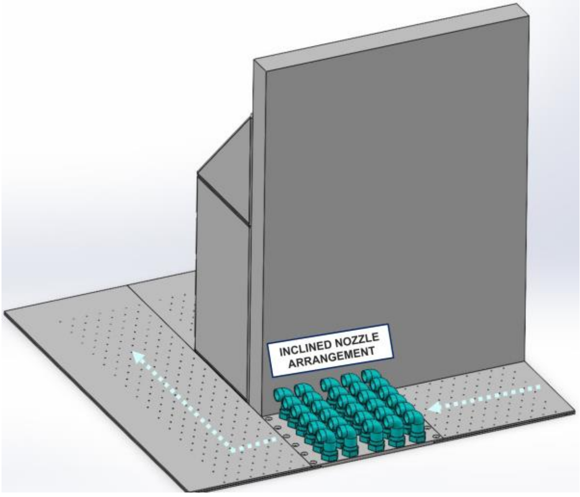
INCLINED NOZZLE ARRANGEMENT

(e) Directed gas injection

Figure 14: Solids conveying configurations tested.

Solids velocity, from which the rate of conveyed solids is derived, is determined using the magnetic solids tracing technique (**Section 3.3.4.** The pressure drops experienced by the injected gas across the conveying module and along the transport channel are measured to analyze the efficiency of converting gas compression energy (see 'E_{IN}' [Eq.(16)]) into net solids flow energy (see 'E_S' [Eq.(15)]).

3.5. Test matrix

This thesis is structured in different sub-studies, as presented in **Section 1.3. Table 5** presents the test matrix employed across the four different studies formulated, outlining the variables that were extracted and analyzed. The investigation encompasses five key operating parameters: fixed bed height, channel width, fluidization number in the transport zone, volumetric flow rate in the conveying zone, and the solids conveying configuration used. These variables were combined according to the set goals in each of the studies. **Table 5** helps in understanding the operational points used in each of them.

Table 5: Overview of the experimental matrix employed in this thesis.

Parameters	**Paper-I**	**Paper-II**	**Paper-III**	**Paper-IV**
Fixed bed height [m]	0.08 – 0.10	0.08 – 0.10	0.08 – 0.10	0.08 – 0.10
Channel width W [m]	0.12	0.12	0.07 – 0.12	0.12
Fluidization number in the transport zone FN_{TZ} [-]	1.83 – 3.00	1.83 – 3.00	3.00	3.00
Volumetric flowrate in the conveying zone Q_{CZ} [m^3/s]	0 – 0.015	0 – 0.015	0 – 0.010	0 – 0.015
Solids conveying configuration [-]	Free solids splashing	Free solids splashing	Directed gas injection	a) Free solids splashing b) Confined solids splashing c) Slugging d) Solids entrainment e) Directed gas injection
Characterization of solids flow				
1. Solids velocity	×	×	×	×
2. Solids dispersion coefficient		×	×	×
3. Fluidization quality		×		
4. Frictional loss			×	
5. Solids conveying efficiency				×

4. Results and discussion

This chapter summarizes the principal findings of the thesis, structured into three sections. **Section 4.1.** assesses the ability of the four proposed measurement methods to quantify the mass flow rate of solids in terms of mean velocity. **Section 4.2.** uses the magnetic solids tracing technique to explore the characterization of solids transport dynamics, encompassing aspects such as solids mean velocity, solids lateral dispersion coefficient, fluidization quality and frictional losses. Lastly, **Section 4.3.** evaluates the performance of different configurations for solids conveying.

4.1. Evaluation of methods for quantifying solids mean velocity

Figure 15 displays the values of solids mean velocity as measured by four different methods, namely: integral mass accumulation, differential mass accumulation, thermal tracing, and magnetic solids tracing. These figures present data across various conditions, aiming to evaluate the response to changes in bed height (H), fluidization number (FN_{TZ}), and the volumetric flow rate of air (Q_{CZ}) in the solids conveying zone. The accompanying vertical bars represent the variance in values across three repetitions under each set of experimental conditions. These bars are present for all data points but may not be visible in some plots due to the small magnitude of the variations.

Overall, all four methods consistently demonstrate the same qualitative trends, with an increase in any of the three operational variables leading to a rise in the solids flow rate. However, the absolute values and the rates of increase vary across methods.

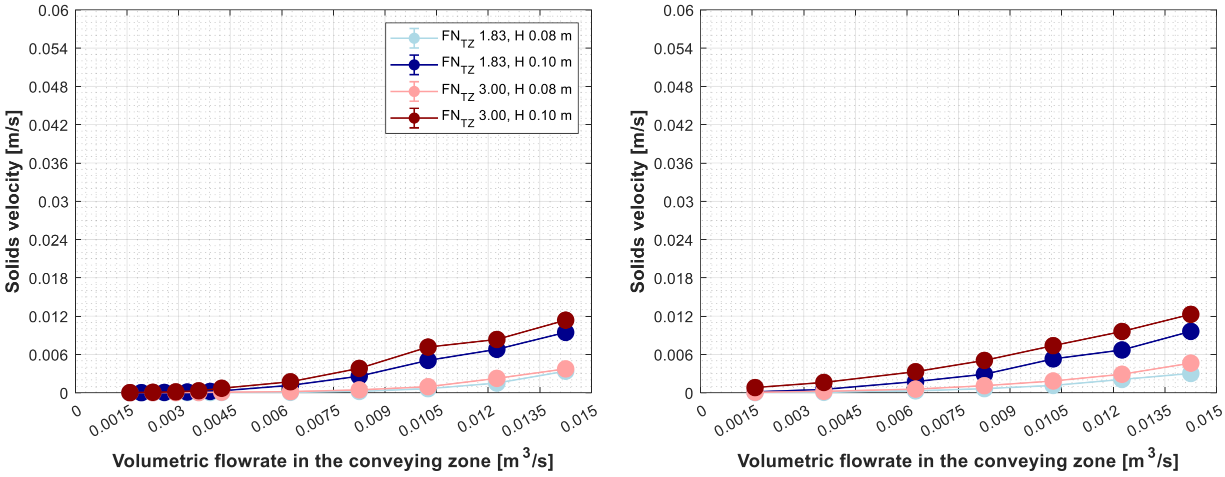

(a) Integral mass accumulation **(b) Differential mass accumulation**

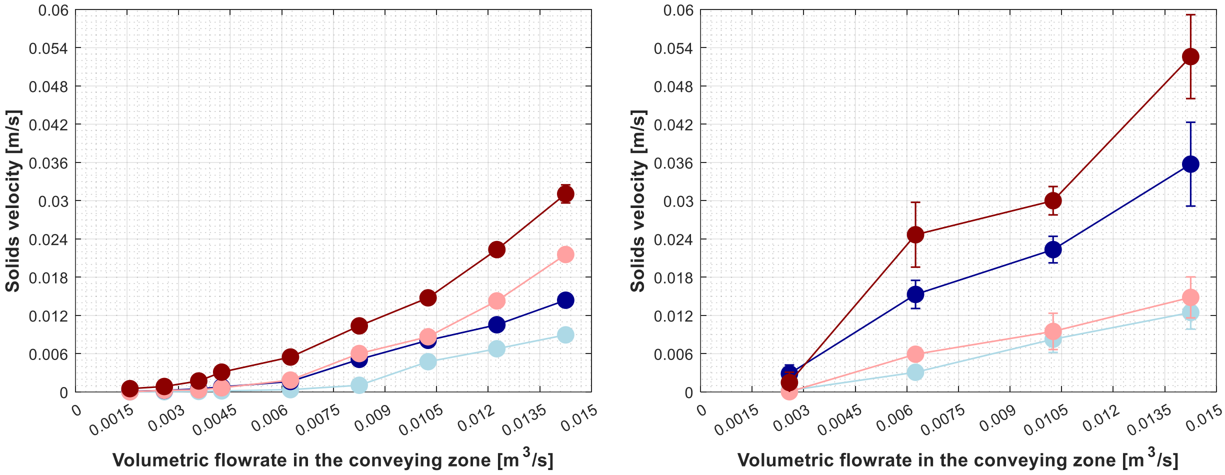

(c) Thermal tracing **(d) Magnetic solids tracing**

Figure 15: Solids velocity measured using four different methods, assessed under different operational conditions. From Paper I.

The two mass accumulation methods yield comparable solids flow rates, generally lower than those obtained with the other methods, likely due to bed material leakage. Among them, the integral method records slightly lower rates than the differential method, making it the lowest on average. Both methods struggle at low solids-conveying rates: the integral method fails to capture low rates because splashed material doesn't attain sufficient height to enter the collection box, while the differential method is affected by ambient noise masking the pressure signal.

The thermal tracing method yields solids flow rates significantly higher (2.5-2.8x) than those obtained by mass accumulation methods. This overestimation is likely due to the thermal method's reliance on temperature data from the bed surface, where solids disperse more rapidly due to bubble splashing compared to the average dispersion throughout the bed height. Thus, the thermal method likely overestimates horizontal dispersion, as demonstrated in **Figure 16**, which compares dispersion values from the thermal and magnetic methods, leading to an underestimation of convection (velocity). Additionally, the barely perceptible spatial gradients of temperature reduce the robustness of the thermal method at high solids flow rates.

Lastly, the magnetic solids tracing method typically provides higher solids flow rates than the other three methods, likely because it avoids the underestimation issues observed in the others. Thus, the magnetic method is deemed to have a superior performance for determining solids flow rate due to its ability to measure continuously (unlike the start-stop procedure required by mass accumulation methods), its consistency and reliability, and its capability to simultaneously assess solids velocity and lateral dispersion.

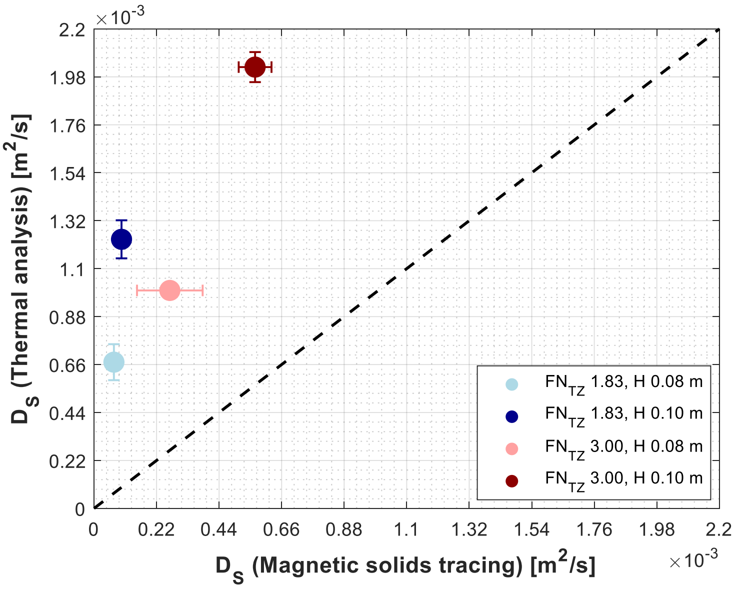

Figure 16: Comparison of solids lateral dispersion coefficient without solids convection: Thermal tracing vs. Magnetic solids tracing analysis.

It is important to clarify the discrepancies between Papers I–II regarding the reported solids velocities obtained through the magnetic solids tracing technique, as shown in **Figure 17**. Regardless of the combination of operating conditions considered, the values reported in Paper I are consistently underestimated compared to those in Paper II. In Paper I, the solids mean velocity is derived from the time delay at the peak data point of the transient tracer concentration profiles. This method's accuracy is limited because it does not account for horizontal solids dispersion, potentially leading to an underestimation of the solids mean velocity. Additionally, identifying the peak time becomes challenging at low solids-conveying rates and under conditions that favor high dispersion, such as increased fluidization velocity or bed height, which increases the uncertainty of the velocity values. In Paper II, the analysis method is improved by considering both the solids velocity and horizontal dispersion coefficient (as explained in **Section 3.3.4.** thereby enhancing reliability. Consequently, the methodology presented in Paper II is used for processing the magnetic solids tracing measurements in Papers III–IV.

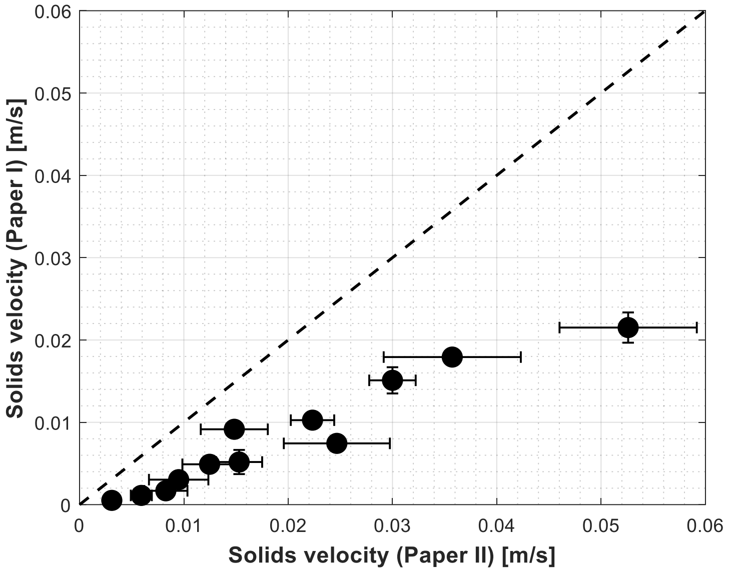

Figure 17: Solids velocity values obtained from the measurements with the magnetic solids tracing technique: comparison of the analysis method in Papers I–II.

Regression analysis was employed to study the influence of operational parameters on solids flow rates across four methods, aiming to further understand the suitability and potential limitations of each technique. **Figure 18** presents factorial effect size statistics, which helps assess the comparative impact of the effects. In all four techniques, the airflow rate in the solids-conveying zone exhibited the most significant influence on solids velocity (factorial effect of 48–60%). Except for the thermal tracing method, the fixed bed height was the second most influential (factorial effect of 36–40%). The fluidization number in the transport zone was the second most influential for the thermal tracing technique (factorial effect size of 25%), but least impactful for the other methods (factorial effect size of 8–12%). The identification of airflow rate supplied to the conveying zone as the most significant factor across all techniques underscores its critical role in controlling solids velocity. The varying influence of bed height and fluidization number across different methods further highlights the importance of method-specific considerations.

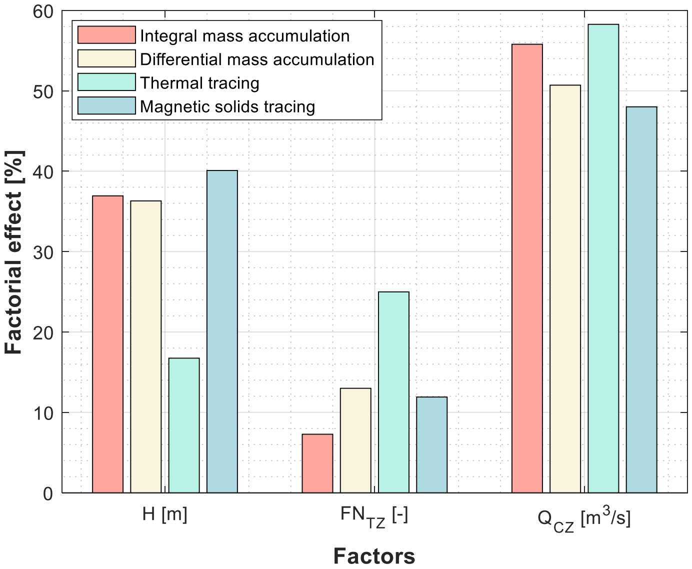

Figure 18: Comparative analysis of factorial effect sizes for the three operational parameters across the evaluated methods. Based on Paper I.

4.2. Characterization of solids transport dynamics

Based on the results in **Section 4.1.** the magnetic solids tracing method was selected to further investigate the characteristics of solids horizontal crossflow. This section is structured into two subsections, each providing insights into different aspects of solids flow parameters. **Section 4.2.1** explores the solids mixing, diving into the relationship between solids velocity and the lateral dispersion coefficient, along with the quality of fluidization. **Section 4.2.2** examines the effect of solids crossflow on frictional losses and presents the findings of rheological analyses.

4.2.1. Solids mixing

Figure 19 illustrates u_S-D_S pairings from all the experimental runs, including three repetitions per operational case. Both parameters—solids mean velocity and solids dispersion coefficient—were derived by fitting the convection-dispersion equation (as explained in **Section 2.1.1**) to the measured tracer concentration curves. The figure includes bars to indicate the confidence interval, defined as the range yielding a 5% increase in the fitting error (refer to Eq. (9) in Paper II). An unexpected key finding is the strong, nearly linear correlation (r=0.804) between horizontal dispersion and solids mean horizontal velocity. This coupling between solids flow and dispersion is likely due to friction-induced shear mixing, which enhances horizontal solids mixing. In operation without solids circulation ($u_S = 0$), an increase in bed height or fluidization number notably boosts the solids horizontal dispersion, corroborating prior studies in stationary bubbling fluidized beds [62]. However, as solids velocity is increased, the influence of bed height on solids dispersion lessens, while the impact of fluidization velocity remains pronounced.

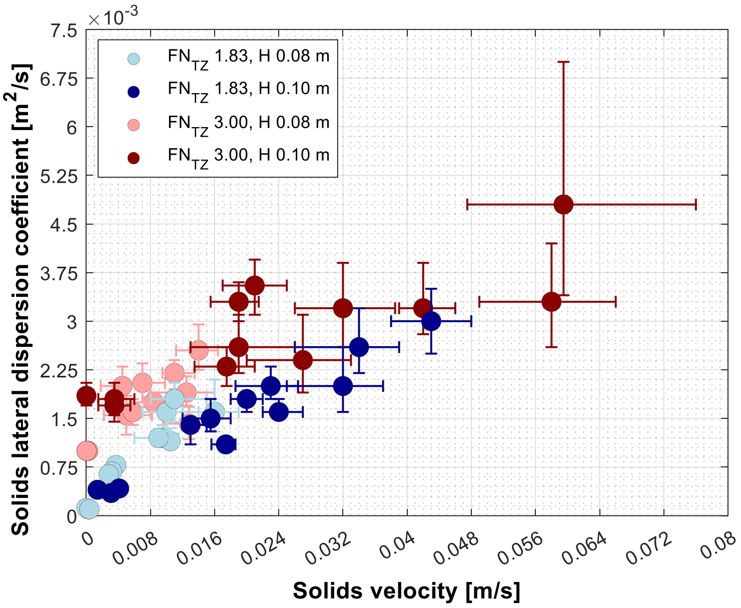

Figure 19: Correlation between solids dispersion and solids velocity for different bed heights (H) and fluidization numbers (FN_{TZ}). Values derived from the convection-dispersion equation. From Paper II.

Figure 20 displays the impact of operational conditions on the fitted values of key parameters of the compartment model used in this study (see **Section 2.1.2**), i.e., the dead zone index (**Figure 20a**) and the number of CSTR tanks in series (**Figure 20b**). Note that these result plots exclude two other parameters extracted from the model fitting: the mean residence time for the PFR and CSTR components. Additionally, in all cases, the calculated values of the PFR component yielded negligible magnitudes, making them insignificant.

The analysis of the dead zone index, as depicted in **Figure 20a**, shows a decreasing trend with the increment of the three operational parameters studied: fluidization number, bed height, and the flowrate of air in the conveying zone. It is important to note that the impact of bed height observed here contrasts with that in stationary bubbling beds, where increased bed height typically worsens gas-solids mixing due to a higher bed-to-distributor pressure drop ratio and larger bubble sizes. However, given the modest bed height range tested in this study, the impact may be minimal and likely masked by other factors. Additionally, the data shows that enhanced solids crossflow more effectively reduces stagnant zones in taller beds than in shallower ones, as the circulation rate increases with bed height (see Paper I). The second parameter 'number of CSTRs arranged in series' (**Figure 20b**) shows a significant increase, primarily influenced by the rate of conveyed solids and increases in the operational parameters—fluidization number and bed height. This indicates a shift from the uniform mixing characteristic of CSTRs towards a plug flow configuration.

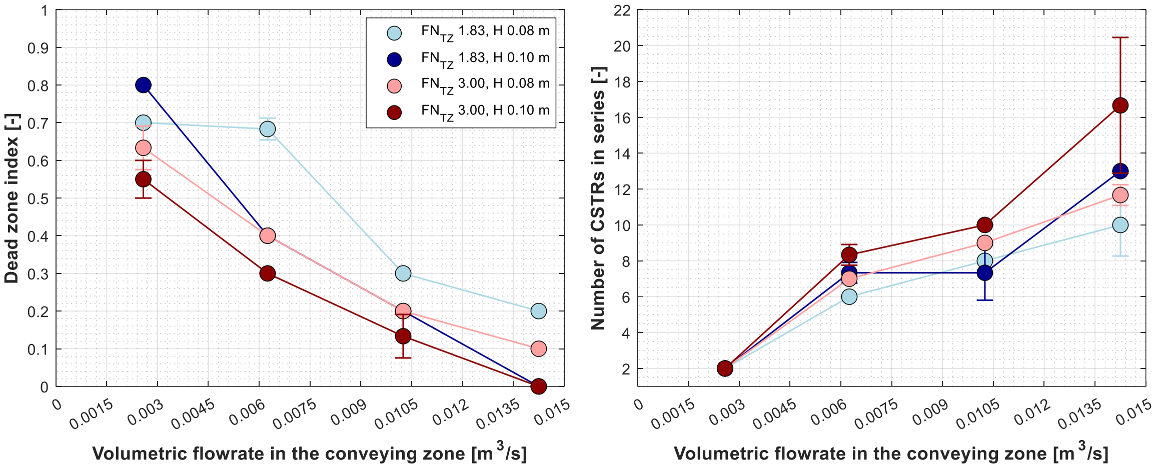

(a) Dead zone index **(b) Number of CSTRs in series**

Figure 20: Impact of operational conditions on the variables extracted after compartment model fitting. From Paper II.

4.2.2. Rheological analysis of solids flow

Figure 21 plots the macroscopic pressure drop gradient established in the direction the solids flow (measurement methodology described in **Section 3.3.5.** against the solids mean horizontal velocity (estimated as described in **Section 3.3.4.** The plot includes data for three different channel widths and three bed heights. An increase in pressure drop with higher solids velocities and narrower channel widths follows the anticipated trend.

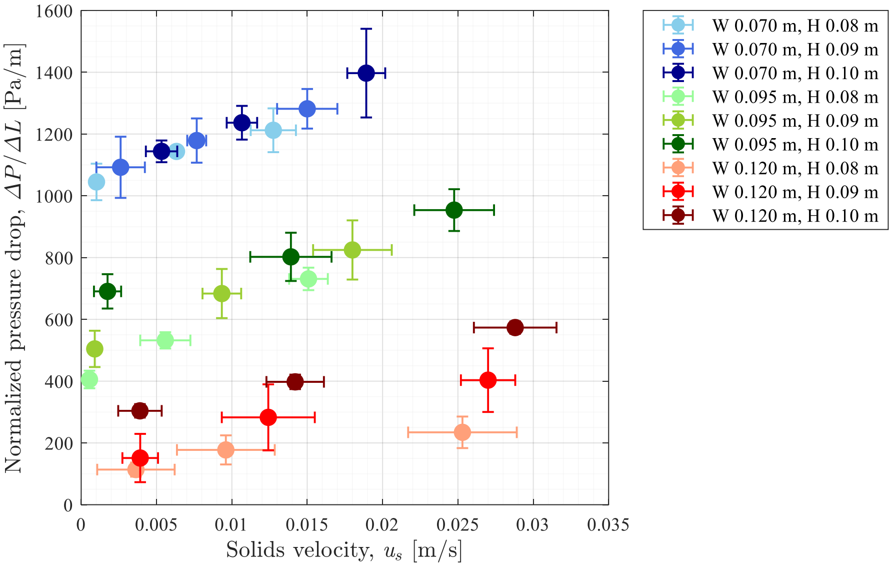

Figure 21: Macroscopic horizontal pressure gradient as a function of solids horizontal velocity. From Paper III.

Aiming to analyze the rheological characteristics of the suspended solids flow, the experimental data in **Figure 21** was processed using rheological models following the methodology outlined in **Section 2.2.1**. **Figure 22a** compares the experimental wall shear stress data with modeled predictions. The R-squared values for the Kozicki et al. [31–34], Kostic-Hartnett [36,37], and Delplace-Leuliet [35] models are 0.314, 0.291, and 0.351, respectively, indicating significant discrepancies between model and experiments. Thus, although these models were developed for single-phase flow in rectangular channels, they have not been tested in gas-fluidized solid systems and show limited applicability, highlighting the need for more appropriate descriptions. Conversely, the new model aligns well with experimental trends, achieving an R-squared value of 0.785, thereby demonstrating a greater ability to describe the experimental data compared to existing models. The results (using data from the newly proposed model in this work), which highlight the relationship between wall shear stress (5–55 Pa) and true wall shear rate (0.002–4.5 s^{-1}), are presented in **Figure 22b**, demonstrating shear thinning behavior.

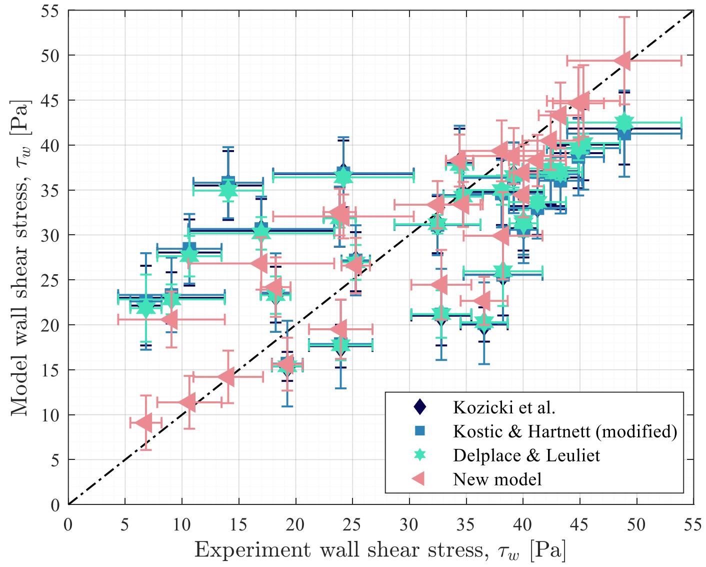

(a) Comparison of modeled & experimental wall shear stress values.

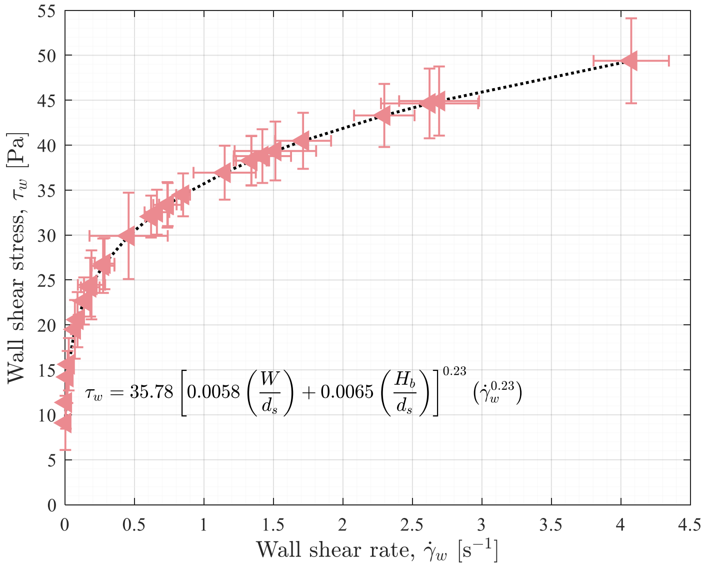

(b) Wall shear stress vs. wall shear rate profile.

Figure 22: Rheological assessment of the non-Newtonian fluid used in the present fluidized bed configuration, exhibiting shear-thinning behavior. From Paper III.

Complementary knowledge in rheological flow characterization involves analyzing the flow by fitting it to a constitutive granular flow model to identify the operating regime, as detailed in **Section 2.2.2**. **Figure 23** illustrates the effective friction coefficient as a function of the inertial number, with a black-dashed line fitting the data according to the $\mu(I)$ constitutive law [Eq.(12)]. The experimental data can be adequately described by the $\mu(I)$ law. The data covers inertial numbers ranging within 10^{-6}–10^{-2} and indicates that the experiments occur in the dense flow regime, with $\mu(I)$ values varying between 0.03–0.3. Thus, both interparticle friction and interparticle collisions play significant roles in momentum transfer within the solids flow.

Note that while the constitutive law fit suggests threshold values for the inertial number and regime shifts, confirming these values requires a broader experimental window not possible with the current setup.

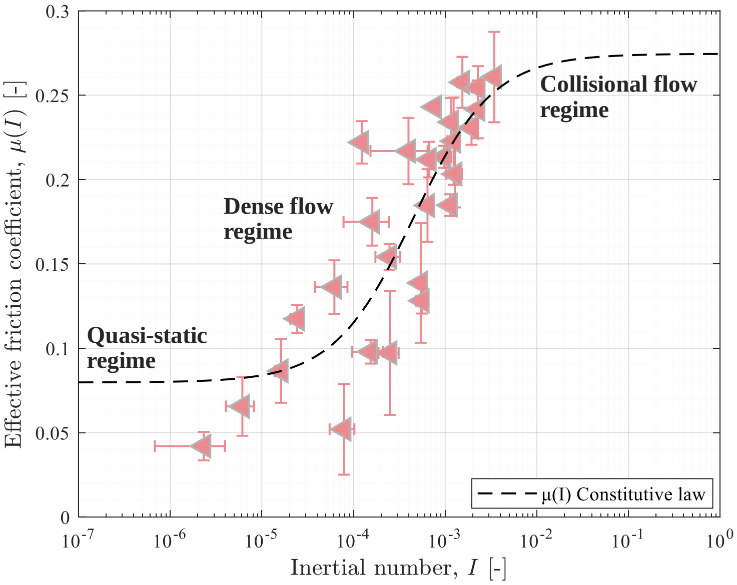

Figure 23: Effective friction coefficient variation with inertial number, fitted with the $\mu(I)$ constitutive law [Eq.(12)] curve. From Paper III.

4.3. Solids conveying efficiency

Figure 24 presents, for each of the five solids-conveying configurations tested, the relationship between the energy flow associated with the mass flow of horizontally conveyed fluidized solids [Eq.(15)] and the energy input into the conveying zone [Eq.(16)], together with the corresponding efficiency. Variations in performance of the different conveying configurations stem from their inherent fluidization dynamics and gas-solids interactions.

The free solids splashing configuration achieves the highest energy transfer efficiency. This is attributed to the macroscopic particle movement in the bubbling regime, where rising and bursting gas bubbles lift and displace particles, transferring substantial kinetic energy in the horizontal direction. In contrast, the confined solids splashing and solids entrainment configurations, characterized by erratic particle motion and fast-moving gas streams, show lower energy transfer efficiencies. In these cases, energy is likely expended in sustaining fluidization and mixing at finer scales, rather than being optimally transferred to solids in the wake of clearly defined bubbles. Lastly, the slugging and directed gas injection configurations deliver intermediate performance, benefiting from solid-gas interactions that are significant but less chaotic than in more turbulent setups. These results emphasize the critical role that configuration and the nature of solid-gas interactions play in determining energy efficiency. Configurations with well-structured gas flows (e.g., clear bubble or slug formations) tend to promote better energy transfer to the solids. Additionally, although bed height generally affects energy efficiency, this impact is most evident in the free solids splashing configuration.

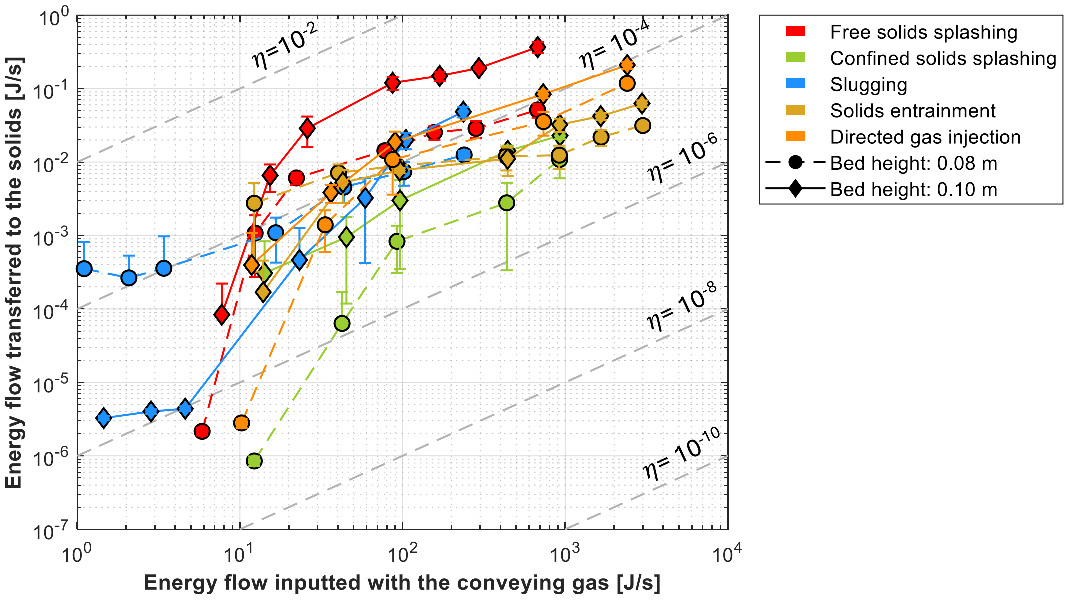

Figure 24: Characterizing conveying zone dynamics in BFB-BFB bed with analysis of energy input and solids energy flux for the five tested configurations. The dashed lines indicate the solids conveying efficiency (η). From Paper IV.

Additionally, when compared to traditional risers in CFB systems, both free splashing and directed gas injection configurations demonstrate higher solids conveying efficiency. These configurations achieve circulation rates at lower fluidization velocities, with solids circulation ranging from 5×10^{-2}–2×10^{3} kg/m^2·s at fluidization velocities of 0.3–4.3 m/s under up-scaled (i.e., 900°C) conditions (see **Figure 10** in Paper IV). This suggests that these tested configurations could provide a more energy-efficient method for driving solids circulation than conventional risers.

5. Conclusion

This thesis investigates the solids flow dynamics in bubbling fluidized beds with induced horizontal solids circulation. A cold-flow model, compliant with Glicksman's simplified set of fluid-dynamic scaling laws, is used. The model features a length scaling factor of 0.12 and is designed to operate at ambient conditions (20 °C, fluidized with air) while simulating hot-scale operation (900 °C) with Geldart B-type particles (silica sand with a mean size of 950 μm).

The study initially evaluates four measurement methods for quantifying the conveyed solids flow rate, a key parameter in the research. These methods include integral mass accumulation, differential mass accumulation, thermal tracing, and magnetic solids tracing. The latter is identified as the most effective due to the resolution and quality of the information acquired, as well as the consistency of the measurements across a considerable range of solids flow rates (Paper-I). Additionally, the impact of three operational parameters—air flow rate for solids conveyance, bed height, and bed fluidization velocity—on the solids flow rate is examined, revealing that an increase in any of these parameters results in a higher solids flow rate. However, the air flow rate in the conveying area has the most significant impact on the rate of solids convection.

Subsequently, measurements from magnetic solids tracing were combined with 1D modeling to elucidate the dynamics of conveyed solids flow (Paper-II). The transient convection-dispersion model accurately described horizontal solids transport, with an average error of 12-18% between modeled and measured solids concentrations across various operational conditions. A roughly linear relationship between the solids dispersion coefficient (1×10^{-4}–5×10^{-3} m²/s) and horizontal velocity (3×10^{-5}–6×10^{-2} m/s) was identified, likely due to shear mixing induced by bed-wall friction. Furthermore, by fitting a compartment model that included parameters such as the dead zone index, residence times in the CSTR and PFR sections, and the number of CSTR reactors in series, the study demonstrated a reduction in the dead zone index—indicating improved fluidization quality—correlated with increased solids crossflow.

The study then examined frictional losses induced by solids crossflow (Paper-III). The normalized pressure gradient (0–1600 Pa/m) in the direction of solids flow showed a non-linear relationship with solids mean horizontal velocity (0–0.035 m/s). Additionally, the solids velocity decreased with transport channel width, confirming the significant influence of bed-wall friction. Pressure drop and velocity measurements yielded wall shear stress values between 5–55 Pa, increasing with wall shear rates between 0.002–4.5 s^{-1}, indicating a clear shear-thinning behavior. Further rheological analysis using the $\mu(I)$-constitutive model categorized the experiments within the dense flow regime, with inertial numbers ranging from 10^{-6} to 10^{-2} and effective friction coefficients between 0.03 and 0.3.

Lastly, the study examines various solids conveying configurations: free solids splashing, confined solids splashing, slugging, solids entrainment, and directed gas injection (Paper-IV). The free solids splashing configuration, operating within the bubbling fluidization regime, proved to be the most efficient in converting the energy input from fluidization gas into horizontal solids transport. Compared to traditional risers in CFB systems, both free splashing and directed gas injection configurations demonstrate higher solids convection efficiency and achieve circulation rates at lower fluidization velocities. Up-scaled solids circulation rates range from 5×10^{-2} to 2×10^{3} kg/m²·s for fluidization velocities of 0.3–4.3 m/s, indicating these methods may offer a more energy-efficient approach to enhancing solids circulation.

6. Future work

Despite its relevance in certain industrial applications, the crossflow configuration in bubbling fluidized beds remains underexplored in the literature. This study has made significant progress, but the complexity of the flow regime calls for further research using advanced measurement techniques and principles from fluid mechanics, reactor design, and fluidization technology.

To better understand the mixing patterns and rheological behavior of solids flow, the fluid dynamics of the gas-solids system can be resolved and validated experimentally through Computational Fluid Dynamics (CFD) modeling. This includes aspects such as gas-solids interaction, quantifying frictional losses, and distinguishing between particle-particle and particle-wall friction.

Another approach to further understanding the system's flow characteristics is the use of advanced measurement techniques, such as sub-millimeter wave range-Doppler radar [64]. In the current study, the magnetic solids tracing technique is used, but it only provides surface-resolved information. Unlike this method, which requires signal conversion to concentration data via a calibration factor, the Doppler radar technique enables the simultaneous acquisition of velocity and concentration profiles.

Nomenclature

A	Cross-sectional area	[m^2]
A_{MZ}	Measurement zone area for solids velocity assessment	[m^2]
Ar	Archimedes number	[-]
a, b	Geometrical parameters, as defined by Kozicki et al. model (see **Table 1**)	[-]
C	Geometrical constant	[-]
C_i	Concentration	[kg/m^3]
$C_{p,F}$	Specific heat capacity of gas	[kJ/kg·K]
$C_{p,S}$	Specific heat capacity of solid particles	[kJ/kg·K]
C_W, C_{H_b}	Geometrical parameters, as defined by the proposed model	[-]
D_h	Hydraulic diameter	[m]
D_S	Solids lateral dispersion coefficient	[m^2/s]
d_S	Mean particle diameter	[μm]
E	Energy flux	[W]
$E(t)$	Exit age distribution	[-]
Fr	Froude number	[-]
f^f	Fanning friction factor	[-]
g	Gravity constant, 9.81	[m/s^2]
H	Bed height	[m]
H_b	Expanded bed height	[m]
I	Inertial number	[-]
I_0	Constant, $\mu(I)$ constitutive law	[-]
i_d	Dead zone index	[-]
k^*	Flow consistency index	[Pa.s$^{n^*}$]
L	Length	[m]
M_t	Mass of solids tracer injected	[kg]
m	Mass	[kg]
N_{CSTR}	Number of reactors in tank-in series component of the compartment model	[-]
n^*	Flow behaviour index	[-]
P	Pressure	[Pa]
ΔP_{TZ}	Pressure drop across the transport zone	[Pa]
P_p	Particle pressure	[Pa]
Q	Volumetric flowrate	[m^3/s]
Re^*	Reynolds number	[-]

T	Temperature	[K]
ΔT	Temperature difference	[K]
t	Time	[s]
u_0	Fluidization velocity	[m/s]
u_f	Gas velocity	[m/s]
u_{mf}	Minimum fluidization velocity	[m/s]
u_S	Solids' velocity	[m/s]
W	Channel width	[m]
x	Horizontal position	[m]
Greek letters:		
β	Geometrical parameter, as defined by the Delplace-Leuliet model (see **Table 1**)	[-]
γ	Isentropic expansion factor	[-]
ε_g	Bed voidage	[-]
η	Solids convection efficiency	[-]
λ	Effective thermal tracing conductivity	[W/m·K]
ρ_B	Bulk density	[kg/m^3]
ρ_f	Density of the bed in fluidized state	[kg/m^3]
ρ_S	Density of solid particles	[kg/m^3]
$\mu(I)$	Effective friction coefficient	[-]
μ_2	Friction coefficient at high inertial numbers, $\mu(I)$ constitutive law	[-]
μ_F	Gas viscosity	[Pa·s]
μ_S	Static friction coefficient, $\mu(I)$ constitutive law	[-]
ξ	Geometrical parameter, as defined by the modified Kostic-Hartnett model (see **Table 1**)	[-]
τ	Mean residence time	[s]
τ_w	Wall shear stress	[Pa]
$\dot{\gamma}_a$	Apparent shear rate	[s^{-1}]
$\dot{\gamma}_w$	Wall shear rate	[s^{-1}]

References

[1] D. Kunii, O. Levenspiel, Fluidization engineering., 2. ed., Butterworth-Heinemann, 1991. https://search.ebscohost.com/login.aspx?direct=true&db=cat09075a&AN=clpc.oai.edge.chalmers.folio.ebsco.com.fs00001000.cfe5a823.1497.4690.b602.bbd293482377&site=eds-live&scope=site&authtype=guest&custid=s3911979&groupid=main&profile=eds.

[2] F. Winter, B. Schratzer, 23 - Applications of fluidized bed technology in processes other than combustion and gasification, in: F. Scala (Ed.), Fluidized Bed Technologies for Near-Zero Emission Combustion and Gasification, Woodhead Publishing, 2013: pp. 1005–1033. https://doi.org/https://doi.org/10.1533/9780857098801.5.1005.

[3] P. Basu, Combustion and gasification in fluidized beds, CRC press, 2006.

[4] J. Grace, X. Bi, N. Ellis, Essentials of Fluidization Technology, Wiley, 2020. https://doi.org/10.1002/9783527699483.

[5] J.G. Yates, Fundamentals of fluidized bed chemical processes, Butterworth Publishers,Stoneham, MA, United States, 1983. https://www.osti.gov/biblio/7129060.

[6] D. S. Pawar, R.K. Surwase, S.B. Bhamare, S.P. Pagar, Fluidized Bed Granulation: A Promising Technique, Int. J Pharm Sci Rev Res 64 (2020) 133–140. https://doi.org/10.47583/ijpsrr.2020.v64i02.022.

[7] M.T. Lim, W.-L. Saw, S. Pang, Effect of fluidizing velocity on gas bypass and solid fraction in a dual fluidized bed gasifier and a cold model, Particuology 18 (2015) 58–65. https://doi.org/https://doi.org/10.1016/j.partic.2014.05.007.

[8] A.R. Bidwe, C. Hawthorne, Y. Xizhi, H. Dieter, G. Scheffknecht, Cold model study of a dual fluidized bed system for the gasification of solid fuels, Fuel 127 (2014) 151–160. https://doi.org/https://doi.org/10.1016/j.fuel.2013.12.020.

[9] M. Yun, Initial Design of a Dual Fluidized Bed Reactor, University of California, Riverside, 2014.

[10] S. Shrestha, B.S. Ali, M.D. Binti Hamid, Cold flow model of dual fluidized bed: A review, Renewable and Sustainable Energy Reviews 53 (2016) 1529–1548. https://doi.org/https://doi.org/10.1016/j.rser.2015.09.034.

[11] X. Wang, J. Lei, X. Xu, Z. Ma, Y. Xiao, Simulation and experimental verification of a hydrodynamic model for a dual fluidized Bed gasifier, Powder Technol 256 (2014) 324–335. https://doi.org/https://doi.org/10.1016/j.powtec.2014.01.087.

[12] S. Bhaskaran, S. Gupta, S. De, Dual Fluidized Bed Gasification of Solid Fuels, in: S. De, A.K. Agarwal, V.S. Moholkar, B. Thallada (Eds.), Coal and Biomass Gasification: Recent Advances and Future Challenges, Springer Singapore, Singapore, 2018: pp. 425–454. https://doi.org/10.1007/978-981-10-7335-9_17.

[13] M. Farha, D.C. Guío-Pérez, F. Johnsson, D. Pallarès, Characterization of the solids crossflow in a bubbling fluidized bed, Powder Technol (2024) 119967. https://doi.org/https://doi.org/10.1016/j.powtec.2024.119967.

[14] O. Levenspiel, Tracer Technology : Modeling the Flow of Fluids, Springer, New York, NY, 2012. https://search.ebscohost.com/login.aspx?direct=true&db=edsebk&AN=567246&site=eds-live&scope=site&authtype=guest&custid=s3911979&groupid=main&profile=eds.

[15] C. Wang, J. Zhu, Developments in the understanding of gas–solid contact efficiency in the circulating fluidized bed riser reactor: A review, Chin J Chem Eng 24 (2016) 53–62. https://doi.org/https://doi.org/10.1016/j.cjche.2015.07.004.

[16] R.L. Pigford, T. Baron, Hydrodynamic stability of a fluidized bed, Industrial & Engineering Chemistry Fundamentals 4 (1965) 81–87.

[17] M. Van de Velden, J. Baeyens, K. Smolders, Solids mixing in the riser of a circulating fluidized bed, Chem Eng Sci 62 (2007) 2139–2153. https://doi.org/https://doi.org/10.1016/j.ces.2006.12.069.

[18] A. Bérard, B. Blais, G.S. Patience, Experimental methods in chemical engineering: Residence time distribution—RTD, Can J Chem Eng 98 (2020) 848–867. https://doi.org/https://doi.org/10.1002/cjce.23711.

[19] P. Ostermeier, F. Fischer, S. Fendt, S. DeYoung, H. Spliethoff, Coarse-grained CFD-DEM simulation of biomass gasification in a fluidized bed reactor, Fuel 255 (2019) 115790. https://doi.org/https://doi.org/10.1016/j.fuel.2019.115790.

[20] F.A. Zenz, D.F. Othmer, Fluidization and fluid-particle systems, in: 1960. https://api.semanticscholar.org/CorpusID:93826163.

[21] M. Farha, D. Carolina Guío-Pérez, F. Johnsson, D. Pallarès, Comparison of solids conveying configurations for fluidized-bed systems, (2024).

[22] J. Baeyens, D. Geldart, Solids mixing, Gas Fluidization Technology (1986) 104.

[23] D. Moslemian, M.M. Chen, B.T. Chao, Experimental and numerical investigations of solids mixing in a gas fluidized bed, Particulate Science and Technology 7 (1989) 335–355.

[24] N. Mostoufi, J. Chaouki, Local solid mixing in gas–solid fluidized beds, Powder Technol 114 (2001) 23–31. https://doi.org/https://doi.org/10.1016/S0032-5910(00)00258-8.

[25] H.K. Versteeg, W. Malalasekera, An introduction to computational fluid dynamics: the finite volume method, 2nd ed, Pearson Education Ltd, Harlow, England ; New York, 2007.

[26] G. Martinez Castilla, A. Larsson, L. Lundberg, F. Johnsson, D. Pallarès, A novel experimental method for determining lateral mixing of solids in fluidized beds – Quantification of the splash-zone contribution, Powder Technol 370 (2020) 96–103. https://doi.org/https://doi.org/10.1016/j.powtec.2020.05.036.

[27] R.P. Chhabra, Bubbles, drops, and particles in non-Newtonian fluids., 2nd ed., CRC Taylor & Francis, 2007. https://search.ebscohost.com/login.aspx?direct=true&db=cat07472a&AN=clec.ybp15915688&site=eds-live&scope=site&authtype=guest&custid=s3911979&groupid=main&profile=eds.

[28] R.P. Chhabra, J.F. Richardson, Non-Newtonian flow and applied rheology : engineering applications., 2nd ed., Butterworth-Heinemann, 2008. https://search.ebscohost.com/login.aspx?direct=true&db=cat09075a&AN=clpc.oai.edge.chalmers.folio.ebsco.com.fs00001000.0bcae914.ea00.4faa.9087.6614c1939e2e&site=eds-live&scope=site&authtype=guest&custid=s3911979&groupid=main&profile=eds.

[29] P. Coussot, Rheometry of pastes, suspensions, and granular materials : applications in industry and environment., Wiley, 2005. https://search.ebscohost.com/login.aspx?direct=true&db=cat09075a&AN=clpc.oai.edge.chalmers.folio.ebsco.com.fs00001000.60becc48.ca9b.4af3.bbc5.aa4210ab8ae8&site=eds-live&scope=site&authtype=guest&custid=s3911979&groupid=main&profile=eds.

[30] A. Bhattad, Review on viscosity measurement: devices, methods and models, J Therm Anal Calorim 148 (2023) 6527–6543. https://doi.org/10.1007/s10973-023-12214-0.

[31] W. Kozicki, C.H. Chou, C. Tiu, Non-Newtonian flow in ducts of arbitrary cross-sectional shape, Pergamon Press Ltd, 1966.

[32] W. Kozicki, C. Tiu, Non-newtonian flow through open channels, Can J Chem Eng 45 (1967) 127–134. https://doi.org/10.1002/cjce.5450450302.

[33] C. Tiu, W. Kozicki, T.Q. Phung, Geometric parameters for some flow channels, Can J Chem Eng 46 (1968) 389–393. https://doi.org/10.1002/cjce.5450460601.

[34] W. Kozicki, C. Tiu, Improved parametric characterization of flow geometries, Can J Chem Eng 49 (1971) 562–569. https://doi.org/10.1002/cjce.5450490503.

[35] F. Delplace, J.C. Leuliet, Generalized Reynolds number for the flow of power law fluids in cylindrical ducts of arbitrary cross, Trends Pharmacol Sci (1995). https://api.semanticscholar.org/CorpusID:78796951.

[36] M.M. Kostic, J.P. Hartnett, Predicting turbulent friction factors of non-newtonian fluids in noncircular ducts, International Communications in Heat and Mass Transfer 11 (1984) 345–352. https://api.semanticscholar.org/CorpusID:120144713.

[37] M. Ayas, J. Skocilas, T. Jirout, A practical method for predicting the friction factor of power-law fluids in a rectangular duct, Chem Eng Commun 206 (2019) 1310–1316. https://doi.org/10.1080/00986445.2018.1557153.

[38] A.B. Metzner, J.C. Reed, Flow of non-newtonian fluids—correlation of the laminar, transition, and turbulent-flow regions, AIChE Journal 1 (1955) 434–440. https://doi.org/10.1002/aic.690010409.

[39] F. Chevoir, J.-N. Roux, F. da Cruz, P.G. Rognon, G. Koval, Friction law in dense granular flows, Powder Technol 190 (2009) 264–268. https://doi.org/https://doi.org/10.1016/j.powtec.2008.04.061.

[40] F. da Cruz, S. Emam, M. Prochnow, J.-N. Roux, F. Chevoir, Rheophysics of dense granular materials: Discrete simulation of plane shear flows, Phys Rev E 72 (2005) 21309. https://doi.org/10.1103/PhysRevE.72.021309.

[41] P. Jop, Y. Forterre, O. Pouliquen, A constitutive law for dense granular flows, Nature 441 (2006) 727–730. https://doi.org/10.1038/nature04801.

[42] G.D.R. MiDi, On dense granular flows, The European Physical Journal E 14 (2004) 341–365. https://doi.org/10.1140/epje/i2003-10153-0.

[43] L.R. Glicksman, Scaling relationships for fluidized beds, Chem Eng Sci 43 (1988) 1419–1421. https://doi.org/10.1016/0009-2509(88)85118-2.

[44] L.R. Glicksman, M. Hyre, K. Woloshun, Simplified scaling relationships for fluidized beds, 1993.

[45] P. Mirek, Influence of the model scale on hydrodynamic scaling in CFB boilers., Brazilian Journal of Chemical Engineering 33 (2016) 885–896. https://doi.org/10.1590/0104-6632.20160334s20150348.

[46] T. Djerf, D. Pallarès, F. Johnsson, Solids flow patterns in large-scale circulating fluidised bed boilers: Experimental evaluation under fluid-dynamically down-scaled conditions, Chem Eng Sci 231 (2021) 116309. https://doi.org/https://doi.org/10.1016/j.ces.2020.116309.

[47] M. Farha, D.C. Guío-Pérez, J. Aronsson, F. Johnsson, D. Pallarès, Assessment of experimental methods for measurements of the horizontal flow of fluidized solids under bubbling conditions, Fuel 348 (2023). https://doi.org/10.1016/j.fuel.2023.128515.

[48] T. Pröll, K. Rupanovits, P. Kolbitsch, J. Bolhàr-Nordenkampf, H. Hofbauer, Cold Flow Model Study on a Dual Circulating Fluidized Bed (DCFB) System for Chemical Looping Processes, Chem Eng Technol 32 (2009) 418–424. https://doi.org/https://doi.org/10.1002/ceat.200800521.

[49] S. Matsuda, Measurement of solid circulation rate in a circulating fluidized bed, Powder Technol 187 (2008) 200–204. https://doi.org/https://doi.org/10.1016/j.powtec.2008.02.004.

[50] A. Gil, C. Cortés, L.M. Romeo, J. Velilla, Gas-particle flow inside cyclone diplegs with pneumatic extraction, Powder Technol 128 (2002) 78–91. https://doi.org/https://doi.org/10.1016/S0032-5910(02)00215-2.

[51] W.-G. Liang, J.-X. Zhu, Y. Jin, Z.-Q. Yu, Z.-W. Wang, J. Zhou, Radial nonuniformity of flow structure in a liquid-solid circulating fluidized bed, Chem Eng Sci 51 (1996) 2001–2010. https://doi.org/https://doi.org/10.1016/0009-2509(96)00057-7.

[52] M.H. Rahman, X.T. Bi, J.R. Grace, C.J. Lim, Comparison of techniques for measuring CFB solids circulation rates at low and high temperatures, Powder Technol 360 (2020) 43–54. https://doi.org/https://doi.org/10.1016/j.powtec.2019.10.033.

[53] W. Zhang, Y. Yan, Y. Yang, J. Wang, Measurement of flow parameters in a bubbling fluidized bed using electrostatic sensor arrays, in: 2015 IEEE International Instrumentation and Measurement Technology Conference (I2MTC) Proceedings, 2015: pp. 1573–1577. https://doi.org/10.1109/I2MTC.2015.7151513.

[54] X.J. Jiang, J.D. Wang, B.B. Jiang, Y. Yang, L.X. Hou, Study of the Power Spectrum of Acoustic Emission (AE) by Accelerometers in Fluidized Beds, Ind Eng Chem Res 46 (2007) 6904–6909. https://doi.org/10.1021/ie070457i.

[55] J.A. Laverman, I. Roghair, M. van S. Annaland, H. Kuipers, Investigation into the hydrodynamics of gas–solid fluidized beds using particle image velocimetry coupled with digital image analysis, Can J Chem Eng 86 (2008) 523–535. https://doi.org/https://doi.org/10.1002/cjce.20054.

[56] B. Wu, A. Kantzas, C.T. Bellehumeur, Z. He, S. Kryuchkov, Multiresolution analysis of pressure fluctuations in a gas–solids fluidized bed: Application to glass beads and polyethylene powder systems, Chemical Engineering Journal 131 (2007) 23–33. https://doi.org/https://doi.org/10.1016/j.cej.2006.12.001.

[57] D.C. Guío-Pérez, F. Dietrich, J.N. Ferreira Cala, T. Pröll, H. Hofbauer, Estimation of solids circulation rate through magnetic tracer tests, Powder Technol 316 (2017) 650–657. https://doi.org/https://doi.org/10.1016/j.powtec.2017.04.062.

[58] J. Porzuczek, Applications of Electrical Capacitance Tomography for Research on Phenomena Occurring in the Fluidised Bed Reactors, Chemical and Process Engineering (2014) 397–408. https://doi.org/10.2478/cpe-2014-0030.

[59] J.F. Davidson, R. Clift, D. Harrison, Fluidization., 2. ed., Academic, 1985. https://search.ebscohost.com/login.aspx?direct=true&db=cat09075a&AN=clpc.oai.edge.chalmers.folio.ebsco.com.fs00001000.1caecdbe.3593.4bd9.a758.6c5fb8dd8859&site=eds-live&scope=site&authtype=guest&custid=s3911979&groupid=main&profile=eds.

[60] F.A. Zenz, D.F. Othmer, Fluidization and fluid-particle systems, in: 1960. https://api.semanticscholar.org/CorpusID:93826163.

[61] M. Leva, Fluidization., McGraw-Hill, 1959. https://search.ebscohost.com/login.aspx?direct=true&db=cat09075a&AN=clpc.oai.edge.chalmers.folio.ebsco.com.fs00001000.8087a3c8.c70b.423f.954b.e7d58d878d8f&site=eds-live&scope=site&authtype=guest&custid=s3911979&groupid=main&profile=eds.

[62] E. Sette, D. Pallarès, F. Johnsson, Influence of bulk solids cross-flow on lateral mixing of fuel in dual fluidized beds, Fuel Processing Technology 140 (2015) 245–251. https://doi.org/10.1016/j.fuproc.2015.09.017.

[63] M. Farha, D. Carolina Guío-Pérez, F. Johnsson, D. Pallarès, Frictional losses in a bubbling fluidized bed with horizontal flow of solids, (2024).

[64] D.C. Guío-Pérez, M. Bonmann, T. Bryllert, M. Seemann, J. Stake, F. Johnsson, D. Pallarès, Radar-based measurements of the solids flow in a circulating fluidized bed, Fuel 345 (2023) 128232. https://doi.org/https://doi.org/10.1016/j.fuel.2023.128232.